

1 **A numerical study of back-building process in a quasi-**  
2 **stationary rainband with extreme rainfall over northern**  
3 **Taiwan during 11-12 June 2012**

4  
5 **Chung-Chieh Wang<sup>1</sup>, Bing-Kui Chiou<sup>1</sup>, George Tai-Jen Chen<sup>2</sup>, Hung-Chi Kuo<sup>2</sup>,**  
6 **and Ching-Hwang Liu<sup>3</sup>**

7 <sup>1</sup> Department of Earth Sciences, National Taiwan Normal University, Taipei, Taiwan

8 <sup>2</sup> Department of Atmospheric Sciences, National Taiwan University, Taipei, Taiwan

9 <sup>3</sup> Department of Atmospheric Sciences, Chinese Culture University, Taipei, Taiwan

10 Correspondence to: C.-C. Wang (cwang@ntnu.edu.tw)

11  
12 **Abstract**

13 During 11-12 June 2012, quasi-stationary linear mesoscale convective systems (MCSs)  
14 developed near northern Taiwan and produced extreme rainfall up to 510 mm and severe  
15 flooding in Taipei. In the midst of background forcing of low-level convergence, the back-  
16 building (BB) process in these MCSs contributed to the extreme rainfall, and thus is  
17 investigated using a cloud-resolving model in the case study here. Specifically, as the cold  
18 pool mechanism is not responsible for the triggering of new BB cells in this subtropical event  
19 during the mei-yu season, we seek answers to the question why the location about 15-30 km  
20 upstream from the old cell is still often more favorable for new cell initiation than other places  
21 in the MCS.

22 With a horizontal grid size of 1.5 km, the linear MCS and the BB process in this case are  
23 successfully reproduced, and the latter is found to be influenced more by the thermodynamic  
24 and less by dynamic effects based on a detailed analysis of convective-scale pressure  
25 perturbations. During initiation in a background with convective instability and near-surface  
26 convergence, new cells are associated with positive (negative) buoyancy below (above) due to  
27 latent heating (adiabatic cooling), which represent a gradual destabilization. At the beginning,  
28 the new development is close to the old convection, which provides stronger warming below

1 and additional cooling at mid-levels from evaporation of condensates in the downdraft at the  
2 rear flank, thus yielding a more rapid destabilization. This enhanced upward decrease in  
3 buoyancy at low levels eventually creates an upward perturbation pressure gradient force to  
4 drive further development along with the positive buoyancy itself. After the new cell has  
5 gained sufficient strength, the old cell's rear-flank downdraft also acts to separate the new cell  
6 to about 20 km upstream. Therefore, the advantages of the location in the BB process can be  
7 explained even without the lifting at the leading edge of the cold outflow.

8

## 9 **1 Introduction**

10 As a common type of mesoscale convective systems (MCSs) with a lifespan around 3-12 h,  
11 organized rainbands such as squall lines are capable of producing persistent precipitation at  
12 high intensity, compared to ordinary, isolated, or scattered convection (e.g., Carbone, 1982;  
13 Bluestein and Jain, 1985; Rotunno et al., 1988; Browning, 1990; Houze et al., 1990; Chen and  
14 Chou, 1993; LeMone et al., 1998; Parker and Johnson, 2000; Doswell, 2001; Johnson and  
15 Mapes, 2001; Sun and Lee, 2002; Weisman and Rotunno, 2004; Meng et al., 2013). When  
16 such rainbands are slow-moving and the embedded deep convective cells travel at small  
17 angles almost parallel to the line, multiple cells can pass through the same locations in  
18 succession to rapidly increase rainfall accumulation and the potential for flash floods (e.g.,  
19 Maddox et al., 1979; Doswell et al., 1996; Brooks and Stensrud, 2000; Parker and Johnson,  
20 2004). For the eastern two thirds of the United States (US), Schumacher and Johnson (2005,  
21 2006) found that 66% of extreme rainfall events there are caused by quasi-linear MCSs,  
22 among which 54% are produced by only two modes in organization. The training line-  
23 adjoining stratiform (TL/AS) type often forms along (or north of) an east-west (E-W) aligned,  
24 pre-existing slow-moving surface boundary (such as a front or a convergence line), and a  
25 series of embedded "training" cells move eastward (also Stevenson and Schumacher, 2014;  
26 Peters and Roebber, 2014; Peters and Schumacher, 2015). The second type is quasi-stationary  
27 back-building (BB) systems, which depend more on meso- and storm-scale forcing and  
28 processes. In BB lines, new cells form repeatedly on the upstream side at nearly the same  
29 location then move downstream, making the line as a whole almost stationary (also Chappell,  
30 1986; Corfidi et al., 1996). While some MCSs may possess characteristics of both types  
31 (Schumacher et al., 2011; Peters and Schumacher, 2015), the BB systems are typically

1 smaller and more localized, and thus more difficult to predict (e.g., Schumacher and Johnson,  
2 2005).

3 To repeatedly trigger new cells in BB MCSs at mid-latitudes, a well-known mechanism is  
4 through convectively-generated outflow boundary from downdrafts, i.e., at the leading edge  
5 of the cold pool (or the gust front) that extends into the upwind side (e.g., Doswell et al., 1996;  
6 Parker and Johnson, 2000; Corfidi, 2003; Schumacher and Johnson, 2005, 2009; Houston and  
7 Wilhelmson, 2007; Moore et al., 2012), sometimes in conjunction with lifting along a frontal  
8 boundary (e.g., Schumacher et al., 2011). Similar mechanisms for the BB process are also  
9 found in some events in the East Asia (e.g., H. Wang et al., 2014; Jeong et al., 2015).  
10 However, toward lower latitudes such as the subtropics and tropics, the environments may be  
11 less conducive to cold pool development (e.g., Tompkins, 2001). Some studies on extreme  
12 rainfall events in South China and Taiwan have shown that surface-based cold air produced  
13 by previous convection that had dissipated for hours or even in the day before, when  
14 impinged by the moist monsoonal flow, in particular the low-level jet (LLJ), can act to trigger  
15 new convection in succession (e.g., Zhang and Zhang, 2012; Xu et al., 2012; C.-C. Wang et  
16 al., 2014a; Luo et al., 2014). Such influences of “cold domes,” however, are different from the  
17 lifting at gust fronts produced by coexisting, dissipating cells or those that had just dissipated,  
18 and the induced MCSs may be less organized if a linear forcing such as a front or low-level  
19 convergence zone is absent (e.g., Xu et al., 2012; C.-C. Wang et al., 2014b).

20 Many heavy rainfall events in Taiwan occur in the mei-yu season (May-June), where repeated  
21 frontal passages affect the area during the transition period from northeasterly to  
22 southwesterly monsoon (e.g., Ding, 1992; Chen, 2004; Ding and Chan, 2005). When the mei-  
23 yu front approaches Taiwan, both the MCSs near the front or those associated with the pre-  
24 frontal LLJ (south of the front) that impinges on the island can bring heavy rainfall (e.g.,  
25 Chen and Yu, 1988; Kuo and Chen, 1990; Wang et al., 2005; C.-C. Wang et al., 2014a).  
26 Under such conditions, BB MCSs may still develop (e.g., Li et al., 1997), in environments  
27 that are not favorable for strong cold pools mainly due to high moisture content at low levels  
28 (e.g., Tompkins, 2001; James and Markowski, 2010; Yu and Chen, 2011). For these systems,  
29 the mechanism for upstream initiation of new cells at the end of the convective line,  
30 presumably also dominated by storm-scale processes as their US counterparts (Schumacher  
31 and Johnson, 2005), is not clear. Recently, the roles of pressure perturbation ( $p'$ ), in particular  
32 the dynamical pressure perturbation ( $p'_d$ , e.g., Rotunno and Klemp, 1982; Weisman and

1 Klemp, 1986; Klemp, 1987, and many others), in the evolution of convective cells inside the  
2 E-W BB rainbands associated with Typhoon Morakot (2009) and extreme rainfall (e.g., Wang  
3 et al., 2012) are examined by Wang et al. (2015, hereafter referred to as WKJ15). They found  
4 that in the presence of an intense westerly LLJ, the interaction between updraft and vertical  
5 wind shear (e.g., Klemp, 1987) induces positive (negative)  $p'_d$  at the western (eastern) flank  
6 of the updraft below the jet-core level (with westerly shear) but a reversed pattern above (with  
7 easterly shear), and thus an upward-directed perturbation pressure gradient force (PGF) at the  
8 western (rear) flank (see e.g., Fig. 6 of WKJ15). This leads to a slow-down in the propagation  
9 speed of mature cells and promotes cell merger inside the rainbands, as often observed in  
10 quasi-linear multi-cell MCSs. A reduced speed of old cell and positive  $p'_d$  at its rear flank  
11 near the surface can also enhance convergence and contribute to upstream new cell initiation  
12 without the cold pool (WKJ15). Obviously, one question worth exploring is whether a  
13 mechanism similar to the Morakot case also plays an important role in other BB rainbands  
14 near Taiwan in the mei-yu season with the presence of a LLJ, or whether some other  
15 processes are also involved? Thus, we seek to further understand and clarify the details of the  
16 BB process in the case below.

17 During 11-12 June 2012, both TL/AS and BB MCSs developed in succession near northern  
18 Taiwan, and produced extreme rainfall up to 510 mm overnight (roughly during 14:00-24:00  
19 UTC 11 June, where LST = UTC + 8 h), in Taipei City and the surrounding metropolitan area.  
20 Many densely-populated urban regions were flooded, and one day (12 June) was declared off  
21 work in Taipei, the first ever in Taiwan in mei-yu season due to heavy rainfall. Thus, this  
22 extreme-rainfall event was rare in its total amount, duration, and location. As will be shown  
23 later, clear BB behavior occurred in the quasi-stationary MCSs and contributed to the extreme  
24 rainfall in northern Taiwan in this event, among other factors linked to frontal forcing and  
25 topographic effects. Thus, this case is studied herein for details in the BB process at the  
26 convective scale, mainly through numerical simulation using a cloud-resolving model at a  
27 horizontal grid size of 1.5 km. Below, the data used and the methodology employed are  
28 described in Sect. 2, and the extreme rainfall event of 11-12 June 2012, including its synoptic  
29 environment, are overviewed in Sect. 3. In Sect. 4, our simulation results are validated against  
30 observations, and further used to investigate the formation mechanism of the linear MCS and  
31 the BB process upstream from the old cells. This evolution is then compared with the  
32 initiation of an isolated cell in Sect. 5 to identify the important factors in the BB process, and  
33 finally the conclusion and summary of this work are given in Sect. 6.

1

## 2 **2 Data and methodology**

### 3 **2.1 Observational data**

4 In this study, the data used include weather maps from the Central Weather Bureau (CWB) of  
5 Taiwan and gridded final analyses ( $0.5^\circ \times 0.5^\circ$ , every 6 h) from the US National Oceanic and  
6 Atmospheric Administration (NOAA)/National Centers for Environmental Prediction (NCEP)  
7 at 26 levels from 1000 to 10 hPa (including the surface level) covering the case period. The  
8 space-borne Advanced Scatterometer (ASCAT; Figa-Saldaña et al., 2002) observations are  
9 also used to assist the analysis of frontal position. For conditions in the pre-storm  
10 environment, the sounding at Panchiao (near Taipei City) is used. For the evolution of the  
11 MCS and the resulting rainfall, the vertical maximum indicator (VMI) composites of radar  
12 reflectivity and hourly data from the rain-gauge network (Hsu, 1998) in Taiwan, both  
13 provided by the CWB, are employed. The above observational data are used both for analysis  
14 and verification of model results.

### 15 **2.2 The CReSS model and experiment**

16 The Cloud-Resolving Storm Simulator (CReSS) is used for our numerical simulation. It is a  
17 cloud-resolving model that employs a nonhydrostatic and compressible equation set and a  
18 height-based terrain-following vertical coordinate (Tsuboki and Sakakibara, 2002, 2007).  
19 Clouds are treated explicitly in CReSS using a bulk cold-rain microphysical scheme (Lin et  
20 al., 1983; Cotton et al., 1986; Murakami, 1990; Ikawa and Saito, 1991; Murakami et al., 1994)  
21 with a total of six species (vapor, cloud water, cloud ice, rain, snow, and graupel). Sub-grid  
22 scale processes parameterized include turbulent mixing in the planetary boundary layer (PBL),  
23 radiation, and surface momentum and energy fluxes (Kondo, 1976; Louis et al., 1981; Segami  
24 et al., 1989). With a single domain (no nesting), this model has been used to study a number  
25 of heavy-rainfall events around Taiwan during the mei-yu season (e.g., C.-C. Wang et al.,  
26 2005, 2011, 2014a,b; Wang and Huang, 2009) as well as for real-time forecasts (e.g., Wang et  
27 al., 2013, 2016a; Wang, 2015, 2016). The CReSS model is open to the research community  
28 upon request, and its further details can be found in the works referenced above and at  
29 [http://www.rain.hyarc.nagoya-u.ac.jp/~tsuboki/cress\\_html/index\\_cress\\_jpn.html](http://www.rain.hyarc.nagoya-u.ac.jp/~tsuboki/cress_html/index_cress_jpn.html).

1 In this study, the simulation is performed using a horizontal grid spacing of 1.5 km and a grid  
 2 dimension (x, y, z) of 1000 × 800 × 50 points (cf. Fig. 1, Table 1). As already described, the  
 3 NCEP 0.5° × 0.5° gridded final analyses serve as the initial and boundary conditions (IC/BCs)  
 4 of the model run from 12:00 UTC 10 June to 12:00 UTC 12 June 2012 (for 48 h). At the  
 5 lower boundary, real terrain at 30 s resolution (or (1/120)°, roughly 900 m) and observed  
 6 weekly sea surface temperature (SST, Reynolds et al., 2002) are provided. The model  
 7 configuration and major aspects of the experiment are summarized in Table 1.

### 8 **2.3 Analysis of vertical momentum and pressure perturbations**

9 To investigate the BB process taking place in the present case using model outputs, the  
 10 methods below, following Wilhelmson and Ogura (1972), Rotunno and Klemp (1982), Klemp  
 11 (1987), and Parker and Johnson (2004), are used to perform analysis of vertical momentum  
 12 and pressure perturbations. With the background environment assumed to be in hydrostatic  
 13 equilibrium, the vertical momentum equation can be written as

$$14 \quad \frac{dw}{dt} = -\frac{1}{\rho} \frac{\partial p'}{\partial z} - \frac{\rho'}{\rho} g + F_z \approx -\frac{1}{\rho_0} \frac{\partial p'}{\partial z} - \frac{\rho'}{\rho_0} g + F_z \quad (1)$$

15 where all variables have their conventional meanings. Here,  $\rho = \rho_0 + \rho'$ , where  $\rho_0$  is the  
 16 background value and  $\rho'$  the perturbation part of  $\rho$ ,  $B = -g(\rho'/\rho_0)$  is the buoyancy, and  $F_z$  is  
 17 the friction term by turbulent mixing. Thus, the vertical acceleration is driven by an imbalance  
 18 among the perturbation PGF, buoyancy, and turbulent mixing. The buoyancy is constituted by  
 19 the gaseous effect and the drag of all condensates, and can be expressed as

$$20 \quad B = -\frac{\rho'}{\rho_0} g = g \frac{\theta'_v}{\theta_{v0}} - g \sum q_x \quad (2)$$

21 where  $\theta_v$  is the virtual potential temperature (and  $\theta_v = \theta_{v0} + \theta'_v$ ) and its perturbation accounts  
 22 for the gaseous effect, while  $q_x$  denotes the mixing ratio of any condensate species.

23 The perturbation pressure  $p'$  can be divided into the dynamical and buoyant components as  $p' = p'_d + p'_b$ , and the diagnostic pressure equations for the anelastic set, with friction omitted  
 24 (e.g., Rotunno and Klemp, 1982; Parker and Johnson, 2004), are

$$26 \quad \nabla^2 p'_b = \frac{\partial}{\partial z}(\rho_0 B) \quad \text{and} \quad (3)$$

$$\nabla^2 p'_d = -\rho_0 \left[ \left( \frac{\partial u}{\partial x} \right)^2 + \left( \frac{\partial v}{\partial y} \right)^2 + \left( \frac{\partial w}{\partial z} \right)^2 - w^2 \frac{\partial^2}{\partial z^2} (\ln \rho_0) \right] - 2\rho_0 \left( \frac{\partial v}{\partial x} \frac{\partial u}{\partial y} + \frac{\partial u}{\partial z} \frac{\partial w}{\partial x} + \frac{\partial v}{\partial z} \frac{\partial w}{\partial y} \right) \quad (4)$$

where  $\nabla^2$  is the laplacian operator. In both equations, a positive (negative) center in  $\nabla^2 p'$  corresponds to a local minimum (maximum) in  $p'$  itself. Equation (3) states that  $p'_b$  is related to the vertical gradient of the product of  $\rho_0$  and  $B$ . On the RHS of Eq. (4), inside the brackets are extension terms which imply maximized  $p'_d$  in regions of nonzero divergence or deformation. The other terms inside the parentheses are shearing terms and imply minimized  $p'_d$  in regions of nonzero vorticity (Parker and Johnson, 2004). The shearing effects include those related to vertical wind shear ( $\partial u/\partial z$  and  $\partial v/\partial z$ ) associated with the LLJ, as reviewed in Sect. 1 for the Morakot case. After  $\nabla^2 p'_b$  or  $\nabla^2 p'_d$  is obtained from Eqs. (3) or (4), the relaxation method is used to solve the associated pressure perturbation through iteration (see Appendix for details).

To provide additional verification, a second, independent method is also used in this study to compute  $p'$  as in WKJ15. In this method,  $p'$  is separated from its background pressure ( $p_0$ ), defined as

$$p_0(x, y, z, t) = \langle p \rangle(x, y, z) + \Delta p(z, t), \quad (5)$$

where  $\langle p \rangle$  is the time-averaged pressure over a fixed period, and  $\Delta p$  is the deviation of the areal-mean pressure  $\bar{p}$  at any given instant from its time mean  $\langle \bar{p} \rangle$ , such that

$$\Delta p(z, t) = \bar{p}(z, t) - \langle \bar{p} \rangle(z). \quad (6)$$

Thus, the gradual decrease of the areal-mean pressure with time as the mei-yu front approaches from the north is reflected in  $\Delta p$ , and taken into account in  $p_0$  besides the spatial variation in mean (time-averaged)  $p$  [cf. Eq. (5)]. Then,  $p'$  is computed simply as

$$p'(x, y, z, t) = p(x, y, z, t) - p_0(x, y, z, t). \quad (7)$$

Referred to as the separation method, it is also applied to other variables to separate the perturbation and the background where needed, such as for  $\rho$  and  $\theta_v$  in Eqs. (1) and (2), as well as potential temperature  $\theta$  and horizontal wind components  $u$  and  $v$ .

26

### 1   **3   Case overview**

#### 2   **3.1   Synoptic and storm environment**

3   In this section, the synoptic conditions and the BB rainbands responsible for the extreme  
4   rainfall are described. Figure 1 shows the surface weather map at 12:00 UTC 11 June 2012,  
5   about 2 h before heavy rainfall started in northern Taiwan. Extending from the East China Sea  
6   to southern China (ENE-WSW), the mei-yu front was about 130 km north of Taiwan, with  
7   almost an upright structure up to 700 hPa in the area. Based mainly on wind field since the  
8   mei-yu front near Taiwan is often associated with strong cyclonic shear vorticity but only  
9   weak thermal contrast (e.g., Kuo and Anthes, 1982; Chen et al., 2003; Wang et al., 2016b),  
10   the frontal position at this time in the NCEP 950-hPa analysis (Fig. 2a) is in agreement with  
11   the surface map, as is the ASCAT observation at 13:00 UTC (Fig. 2e). In the NCEP analysis,  
12   the strong southwesterly LLJ south of the front over the Taiwan Strait and off southeastern  
13   Taiwan is also revealed. While the LLJ reaches  $20 \text{ m s}^{-1}$  in maximum speed (at 950 hPa), the  
14   axis over the strait points toward northwestern Taiwan between the front and the island's  
15   topography (Fig. 2a). When the mei-yu front approaches and the prevailing southwesterly  
16   flow strengthens (mainly due to an increased pressure gradient), such a configuration is often  
17   produced in response to flow splitting due to terrain blocking and the subsequent channeling,  
18   confluence, and acceleration, with local wind maxima, i.e., barrier jets, near the two ends of  
19   Taiwan (e.g., Li and Chen, 1998; Wang and Chen, 2002; Chen et al., 2005). For the one in  
20   northern Taiwan Strait (Fig. 2a), in particular, the low-level convergence (from confluence)  
21   associated with the barrier jet can provide the forcing for quasi-linear MCSs near or south of  
22   the front (e.g., Yeh and Chen, 2002; Wang et al., 2005). The NCEP analyses every 6 h shows  
23   that the 950-hPa front reached northern Taiwan near 00:00 UTC 12 June (Fig. 2c), also  
24   consistent with ASCAT data at 02:00 UTC (Fig. 2f). Afterward, as the rainfall in northern  
25   Taiwan gradually weakened (cf. Figs. 4 and 9, to be discussed later), the mei-yu front  
26   advanced rapidly across Taiwan and reached about  $23^\circ\text{N}$  within 6 h (Fig. 2c).

27   The Panchiao sounding (Fig. 3) in the Taipei metropolitan area (cf. Fig. 2c) at 12:00 UTC 11  
28   June indicated very strong southwesterly flow throughout the lower troposphere, with a peak  
29   of  $25 \text{ m s}^{-1}$  near 925 hPa, consistent with the barrier jet in Fig. 2a (also e.g., Li and Chen,  
30   1998; Chen et al., 2005). Near the surface, the temperature lapse rate was close to dry adiabats  
31   and indicated a well-mixed profile, while that further aloft was less steep but still mostly



1 exceeded the moist adiabats, indicating conditional instability up to about 550 hPa. The  
2 convective available potential energy (CAPE) was  $583 \text{ J kg}^{-1}$  and sufficient to support deep  
3 convection, if the air parcel could overcome the convective inhibition (CIN) of  $78 \text{ J kg}^{-1}$  to  
4 reach the level of free convection at 789 hPa. Obviously, these conditions were soon met  
5 since heavy rainfall did occur in Taipei. Note also that the humidity was quite high below  
6 about 550 hPa, and a dry layer did not exist throughout the troposphere. Thus, with instability  
7 and low-level convergence, the strong, deep, and moisture-laden southwesterly flow near and  
8 to the south of the approaching mei-yu front was clearly very favorable for active convection  
9 and substantial rainfall (e.g., Jou and Deng, 1992; C.-C. Wang et al., 2014a).

### 10 **3.2 The back-building rainband with extreme rainfall**

11 Figure 4 presents the composite VMI radar reflectivity from the ground-based radars in  
12 Taiwan at 1 h intervals, and depicts the evolution of the rainbands causing the extreme rainfall  
13 in northern Taiwan. At 12:00 UTC 11 June (Fig. 4a), an intense ENE-WSW-oriented squall  
14 line, with peak reflectivity in convective elements  $\geq 50 \text{ dBZ}$ , already formed and was  
15 approaching northern Taiwan to within about 30 km, i.e., at some 80-100 km ahead of the  
16 surface mei-yu front (cf. Figs. 1 and 2a). With a bulging middle section and trailing stratiform,  
17 the squall line moved southward at about  $15 \text{ km h}^{-1}$  and into northern Taiwan by 14:00 UTC  
18 (Fig. 4b and c). During the following hours through 18:00 UTC, this squall line continued to  
19 advance slowly and into  $25^\circ\text{N}$ , so that much of the northern Taiwan was covered by echoes  
20 with high reflectivity (Fig. 4d-g), while the stratiform region gradually moved eastward, in  
21 agreement with the upper-level wind (cf. Fig. 3). After 18:00 UTC, the convection through  
22 northern Taiwan evolved into a narrow line that remained quasi-stationary for hours until  
23 23:00 UTC (Fig. 4g-l), with evident new development toward the west, i.e., back-building  
24 behavior (to be detailed later). Eventually, this linear MCS started to move south slowly and  
25 gradually away from the Taipei area after 00:00 UTC 12 June (Fig. 4m-o), likely in  
26 conjunction with the surface front with the arrival of the northeasterly flow (cf. Fig. 2c and f).  
27 During the entire period of Fig. 4, the mountain interiors in central and southern Taiwan also  
28 received continuous rainfall from forced uplift of the strong LLJ by the topography (cf. Fig.  
29 2a and c), and another squall line also approached southern Taiwan from the west and made  
30 landfall near 22:00 UTC 11 June (Fig. 4i-o). Nonetheless, the reflectivity over northern  
31 Taiwan was both very active and lengthy, and produced by two types of MCSs: the first was

1 the squall line before 18:00 UTC 11 June and reminiscent to a TL/AS system, and the second  
2 was the quasi-stationary BB MCS after 18:00 UTC (Fig. 4).

3 The distributions of 6 h accumulated rainfall during 12:00-18:00 and 18:00-24:00 UTC 11  
4 June are shown in Fig. 5a and b. While three distinct rainfall centers over northern, central,  
5 and southern Taiwan were produced in each period, the amount over northern Taiwan was the  
6 highest. The rainfall during 12:00-18:00 UTC was maximized along the northwestern coast  
7 and decreased inland (Fig. 5a), consistent with the MCS that moved in from the ocean (cf. Fig.  
8 4). On the other hand, the rainfall was more concentrated during 18:00-24:00 UTC with  
9 almost an E-W alignment, and the center was right near the Taipei City (Fig. 5b). The peak  
10 amount during this later 6 h period was 311 mm, and an extreme value of 510 mm was  
11 recorded overnight from the entire event. It is perhaps worthy to note that the mountainous  
12 interior in central and southern Taiwan also received heavy rainfall since about 00:00 UTC 10  
13 June (presumably due to forced uplift), but little rain fell over northern Taiwan prior to the  
14 current event.

15 While back-building likely also occurred in the TL/AS-type squall line, such behaviors in the  
16 quasi-stationary rainband after 18:00 were well depicted by the radar VMI reflectivity every  
17 10 min (Fig. 6). As marked by the short arrows, frequent BB activities can be spotted at the  
18 western end of the convective line or west of existing mature cells, and some of them were  
19 quite close to the northwestern coast of Taiwan. After formation, they moved at small angles  
20 from the ENE-WSW-oriented quasi-stationary line, repeatedly across northern Taiwan with  
21 frequent cell mergers similar to those in WKJ15 (Fig. 6). The resulted rainfall in Fig. 5b, with  
22 the maximum located inland near Taipei, also implies that many cells matured after they  
23 moved onshore instead of over the ocean prior to landfall. Since the length of the line with  
24 active cells upstream from Taipei is about 160 km and most cells travelled at the speed range  
25 of 60-80 km h<sup>-1</sup> in Fig. 6, the heavy rainfall would last only 2-2.5 h and much shorter than in  
26 reality (cf. Fig. 5), if there were no new developments westward along the line.

27 In extreme events, there are often multiple factors of different scales working in synergy to  
28 lead to their occurrence. This is also true in the present case, and the scenario leading to heavy  
29 rainfall can be quite complicated. While the large and synoptic scale conditions provided a  
30 favorable background (Figs. 1-3), the two MCSs developed south of the approaching mei-yu  
31 front, in close proximity to the area of terrain-influenced low-level convergence (and the  
32 barrier jet) near northern Taiwan (Figs. 2a, c, e, and f, and 4). In Figs. 4 and 6, the convective

1 lines even exhibited characteristics of multiple lines at times, possibly linked to gravity wave  
2 activities (e.g., Yang and Houze, 1995; Fovell et al., 2006). While the formation mechanism  
3 of the quasi-linear MCSs (the second one in specific) and the roles played by both the mei-yu  
4 front and the topography will be discussed and clarified (Sect. 4.2), the BB process at the  
5 convective scale was also a contributing factor to the extreme rainfall, especially during the  
6 later 6 h period after 18:00 UTC (Fig. 6). Also, as typical in many events, the new BB cell is  
7 often found to develop about 15-30 km upstream from an old cell in Fig. 6. Thus, why this  
8 particular spot has an advantage for new cell initiation compared to other locations without a  
9 nearby old cell, is the scientific question that we wish to answer and the main focus of this  
10 case study. This specific question (and the formation mechanism of the MCSs) will be  
11 addressed through our numerical simulation results below.

12

## 13 **4 Results of model simulation**

### 14 **4.1 Model result validation**

15 As described in Sect. 2.2, our CReSS model simulation was performed from 12:00 UTC 10  
16 June 2012 for 48 h using NCEP (0.5°) final analyses as IC/BCs, with a horizontal grid spacing  
17 of 1.5 km. The simulated winds and the front at an elevation of 549 m (close to 950 hPa) at  
18 12:00 UTC 11 June ( $t = 24$  h) and frontal positions every 6 h are shown in Fig. 2b and d.  
19 Compared to the observation and NCEP analyses (Figs. 1, 2a, and 2e), the simulated front in  
20 Fig. 2b is slightly too north, especially west of 120.5°E and over land in southeastern China,  
21 but the prefrontal LLJ is well captured, including the strong winds (barrier jet) near northern  
22 Taiwan. Linked to the position error of the front at 12:00 UTC, the modeled front is also too  
23 north at 18:00 UTC, but its western segment over the strait advanced southward more rapidly  
24 to catch up with the NCEP analyses during the next 6 h (Fig. 2c and d). The segment east of  
25 Taiwan, however, is still too north at 00:00 UTC 12 June (cf. Fig. 2f) and the position error  
26 there does not improve until about 12 h later (Fig. 2c and d).

27 The model-simulated surface winds at 10 m height and column-maximum mixing ratio of  
28 total precipitation every 2 h during 12:00-22:00 UTC 11 June are shown in Fig. 7, which can  
29 be compared with the radar composites in Fig. 4. In the model, the squall line before 18:00  
30 UTC is along and to the north of the near-surface front (Fig. 7a-d) and different from the  
31 training-line system ahead of the front in the observation. Thus, the simulation of the first

1 MCS was not ideal in location, apparently linked to the frontal position error discussed earlier.  
2 On the other hand, the quasi-stationary MCS over northern Taiwan since 18:00 UTC, with  
3 intense convective cells near Taipei, as well as the second squall line over the southern strait,  
4 are both nicely captured in the model as the front advanced south (Fig. 7d-f). As a result, the  
5 rainfall simulation in northern Taiwan during 18:00-24:00 UTC, with a peak amount of 312  
6 mm, is in close agreement with the observation (Fig. 5b and d), while that during the  
7 preceding 6 h was not (Fig. 5a and c). Similar results are also revealed by hourly histogram of  
8 rainfall in Fig. 8, averaged inside the elongated box depicted in Fig. 5b. The rainfall in  
9 northern Taiwan was much better simulated in magnitude and variation in time after 18:00  
10 UTC 11 June (Fig. 8), although the areal-averaged intensity in the model is somewhat lower  
11 because the simulated rain belt is narrower than the one observed (Fig. 5b and d). Also, the  
12 model predicted more rainfall than observed over the mountains in southern Taiwan (Fig. 5),  
13 indicating that the flow over the terrain might be somewhat over-estimated, though this is not  
14 our focus here.

## 15 **4.2 Formation of the quasi-linear MCS**

16 The more detailed distributions of horizontal winds and convergence/divergence near the  
17 surface at 312 m from 18:30 to 21:00 UTC 11 June 2012 in the model are shown in Fig. 9.  
18 With a wavy pattern and strong convergence along most of its length, the near-surface mei-yu  
19 front (black dotted curves) is north of Taiwan but gradually approaches during this period.  
20 Consistent with Figs. 1, 2, 6, and 7, the quasi-linear and stationary MCS, on the other hand,  
21 developed south of the front near 25°N. As the front advances, their distance decreased from  
22 about 90 km at 18:30 UTC to 30 km at 21:00 (Fig. 9), and in the observation the front only  
23 caught up with the pre-frontal MCS after 00:00 UTC 12 June as mentioned (cf. Figs. 2c and  
24 4g to o). Crossing northern Taiwan, the rainband forms along a near-surface convergence  
25 zone (green dotted curves, mostly  $> 5 \times 10^{-5} \text{ s}^{-1}$  with confluence and acceleration) between  
26 the flow blocked and deflected northward by the topography of Taiwan and the unblocked  
27 flow farther to the north and west in the environment (but still ahead of the front, Fig. 9).  
28 Thus, in agreement with the observations, the effects of terrain (blocking) appeared to play a  
29 key role to initiate the rainband development, while the front helped provide and channel an  
30 enhanced background flow with its approach in the present case. Such a scenario is quite  
31 similar to those studied by Yeh and Chen (2002) and Wang et al. (2005). Thus, the frontal  
32 forcing, LLJ, terrain effects, and the BB process all work together to lead to the quasi-linear

1 MCS and heavy rainfall in northern Taiwan in the present case. However, it is not possible to  
2 isolate and quantify their individual contribution here, nor do we intend to do so.

3 Figure 10 shows the development and evolution of convective cells over northern Taiwan and  
4 the upstream area in the model every 10 min during 19:20-22:10 UTC. In this quasi-stationary  
5 system (cf. Figs. 7d-f and 9), the BB process is successfully simulated by CReSS. For  
6 example, a new cell labeled as “A2” develops about 20 km upstream from the old cell “A1”  
7 around 19:30 UTC, and becomes mature near 20:10 UTC. Likewise, “B2” is triggered west of  
8 “B1” after 21:20 UTC, and develops into a mature cell near 21:40 UTC and then the two cells  
9 merge near 21:50 UTC over northern Taiwan (Fig. 10, also cf. Fig. 9), in a way similar to that  
10 discussed by WKJ15. In the model, the training of multiple cells in succession clearly leads to  
11 heavy rainfall over the Taipei area (cf. Fig. 7e and f), in agreement with the observations.  
12 Therefore, even though the simulation of the first TL/AS MCS is less than ideal, the model  
13 results for the quasi-stationary BB lines (after about 18:00 UTC 11 June) can be used to  
14 further investigate the BB process upstream from the old cells in this case. Thus, the area and  
15 time period selected for the separation of  $p_0$  and  $p'$ , as described at the end of Sect. 2.3, are set  
16 to 24.75-25.15°N, 120.35-121.75°E (cf. Fig. 7a) and over 18:00-24:00 UTC 11 June 2012.

### 17 **4.3 Structure of convective cells in the BB MCS**

18 In this subsection, the simulated structure of convective cells inside the BB system is first  
19 examined, before the discussion on the finer details of pressure perturbations and their  
20 associated effects in the BB process. The pair of old and new cells for study has been chosen  
21 to be B1 and B2 over the period of 20:00-21:40 UTC, as they are farther away and less  
22 affected by the terrain of northern Taiwan (cf. Fig. 10). To reveal the storm environment  
23 (provided by the background forcing), E-W vertical cross-sections along 25°N through the  
24 centers of both B1 and B2 (line AB in Fig. 10) are constructed and averaged over three  
25 outputs from 21:25 to 21:35 UTC, as shown in Fig. 11a. The equivalent potential temperature  
26 ( $\theta_e$ ) has a minimum of about 350 K at mid-levels (near 4-5 km) and increases both upward  
27 and downward in upstream as well as downstream regions, indicating the presence of  
28 convective (and conditional) instability (cf. Fig 3). During the average period, the mean  
29 updraft of B1 is located near 121.35°E (cf. Fig. 10), and its immediate upstream region, i.e.,  
30 where cell B2 is developing (~121.2°E), is characterized by strong near-surface convergence  
31 coupled with upper-level divergence (Fig. 11a). Clearly favorable for new cell development

1 upstream with near-surface convergence there, such a thermodynamic and kinematic structure  
2 under the influences of the front and terrain (as discussed in Sect. 4.2) is very similar to the  
3 composites of BB MCSs in the USA obtained by Schumacher and Johnson (2005, their Fig.  
4 17b). The WSW-ENE cross-section (along low-level flow) through B1 about 30 min earlier at  
5 21:00 UTC shows a gradual acceleration of the upstream LLJ (thick arrow line) under the  
6 forcing of background convergence. As the jet approaches B1, which is already in mature  
7 stage (and quasi-steady), there is a rapid local acceleration then intense deceleration across B1,  
8 by about  $10 \text{ m s}^{-1}$  with a convergence in excess of  $5 \times 10^{-3} \text{ s}^{-1}$  (Fig. 11b). While this local  
9 acceleration is clearly a response to the development of B1, the resulting vertical wind shear  
10 from the south-southwest is strongest below 500 m under B1 and its immediate upstream,  
11 where a value of about  $2\text{-}3 \times 10^{-2} \text{ s}^{-1}$  can be reached (Fig. 11c). The vertical wind shear  
12 upstream from B1 further aloft turns into northerly and then northeasterly at about 2 km, as  
13 expected above the axis of the LLJ, but its value ( $\sim 3 \times 10^{-3} \text{ s}^{-1}$ ) is one order of magnitude  
14 smaller (Fig. 11c). Thus, the vertical wind shear in the storm environment of B1 (and B2) is  
15 strongest near the surface. Also, the deep convection can be seen to tilt eastward with height  
16 in both cross-sections, consistent with the direction of the upper-level winds and the evolution  
17 of stratiform area (cf. Figs. 3 and 4).

18 In Fig. 12, the perturbations in  $\theta$  (i.e.,  $\theta'$ ) and horizontal winds ( $u'$  and  $v'$ ) obtained through  
19 the separation method (cf. Sect. 2.3), as well as the associated convergence and divergence,  
20 surrounding the pair of cells B1 and B2 at the surface between 20:00 and 21:00 UTC are  
21 presented every 20 min. During this initiation period of B2, while there exists positive  $\theta'$  (of  
22 0.4-0.8 K) below the updraft of B1, its induced cold pool is very weak at the surface, with a  $\theta'$   
23 of only  $-0.3 \text{ K}$  at most, and is roughly 10 km to the east at the forward flank (Fig. 12). The  
24 convergence at the leading edge of the diverging, marginally colder air (denoted by dotted  
25 curves) extends to the southeast and south of B1 at 20:00-20:20 UTC (Fig. 12a and b), but  
26 gradually moves to the east afterwards (Fig. 12c and d). At the rear side of B1, the new cell  
27 B2 (marked by a blue "x") develops inside a region of surface convergence, consistent with  
28 Fig. 9d, e, and f, and quite far (at least 10 km) from both the weak cold pool and the leading  
29 edge of its outflow (Fig. 12). Therefore, the cold pool does not play any significant role in the  
30 initiation of the back-building cell B2 in the model, and the B1-B2 pair appears to be ideal for  
31 further investigation in greater detail.

1 The results of  $\nabla^2 p'$  obtained by the two different methods (by separation and from Eqs. 3 and  
2 4) as described in Sect. 2.3 at two different heights near 0.8 and 3 km are compared in Fig. 13,  
3 also for 21:00 UTC as an example. In general, the patterns are very similar. At 0.8 km,  
4 negative  $\nabla^2 p'$  (implying  $p' > 0$ ) occurs near the updraft of B1 with positive  $\nabla^2 p'$  (implying  $p'$   
5  $< 0$ ) to the east near the downdraft (Fig. 13a and b). West of B1 where B2 is developing,  
6 positive (negative)  $\nabla^2 p'$  is found to the south (north) of the near-surface convergence zone.  
7 Near 3 km, the updraft of B1 corresponds to  $\nabla^2 p' > 0$  and  $\nabla^2 p' < 0$  occurs to its western flank  
8 and further upstream over B2 (Fig. 13d and e). The laplacian of buoyancy pressure  
9 perturbation ( $\nabla^2 p'_b$ ) alone computed from Eq. (3) closely resembles that of the total pressure  
10 perturbations at both levels (except perhaps a slight southward shift near the updraft of B1 at  
11 0.8 km), implying a dominant role of  $p'_b$  over  $p'_d$  in this event. Nevertheless, Fig. 13 confirms  
12 that the two methods yield consistent results.

#### 13 **4.4 Analysis of pressure perturbations**

14 To examine the distributions of pressure perturbations and their roles in the BB process in  
15 greater detail, a series of vertical cross-sections through the updraft center of B1 at 5 km and  
16 the near-surface center of B2 from 20:00 to 21:00 UTC (each roughly 50 km in length, cf.  
17 Figs. 10 and 12), i.e., during the initiation stage of B2, are constructed. Here, the structures of  
18  $\nabla^2 p'$  are first presented, so as to better infer to the patterns of  $p'$  discussed later through Eqs.  
19 (3) and (4). At 20:00 UTC when signs of B2 are yet to appear (Fig. 14a), the updraft of B1  
20 ( $>5 \text{ m s}^{-1}$ ) is more upright with downdrafts at both flanks ( $>1 \text{ m s}^{-1}$  at mid-level or above). At  
21 the backside (upstream) of the updraft, in particular,  $\nabla^2 p'$  is positive at mid-level and negative  
22 both above and below, corresponding to  $p' < 0$  and  $p' > 0$ , respectively (as labeled by “L” and  
23 “H”). Again, the pattern of  $\nabla^2 p'$  is largely attributable to its buoyant ( $\nabla^2 p'_b$ ) instead of  
24 dynamical component ( $\nabla^2 p'_d$ , Fig. 14b and c). Twenty minutes later at 20:20 UTC (Fig. 14d),  
25 the updraft of B1 strengthens to more than  $8 \text{ m s}^{-1}$  and becomes more tilted, but the basic  
26 pattern of  $\nabla^2 p'$  at its western flank and the upstream region remains. At this time, the  
27 suppressing downdraft there weakens, and B2 is developing ( $\sim 0.5 \text{ m s}^{-1}$ ) just west of the  
28 sinking motion and about 15 km upstream from the core of B1. This new development is  
29 associated with  $p' < 0$  below 1 km and  $p' > 0$  over 1-3 km, and the perturbations (and those of  
30 B1) are also mainly from the buoyant rather than dynamical effects (Fig. 14e and f).

1 At 20:40 UTC (Fig. 14g), B1 further strengthens and is even more tilted with height, and its  
 2 associated downdraft below the mid-level ( $> 2 \text{ m s}^{-1}$  near 4 km) now appears only at the  
 3 eastern (downwind) side (cf. Fig. 12c). The upward motion of B2 can now reach over  $1 \text{ m s}^{-1}$   
 4 and extend further upstream, while a layer of positive  $\nabla^2 p'$  (implying  $p' < 0$ ) forms near 5 km,  
 5 again mainly from the buoyant effects (cf. Fig. 14h). The distribution of  $\nabla^2 p'_d$  is only  
 6 significant at both flanks of the updraft of B1 below about 3.5 km (and at its eastern flank  
 7 near 5 km, Fig. 14i), which forms gradually as B1 intensifies (Fig. 14c and f). The  
 8 configuration of positive (negative)  $p'_d$  at the rear (forward) flank of the updraft near 500 mm  
 9 (below the jet level, cf. Fig. 11c) and a reversed pattern above (near 2-3 km) is consistent with  
 10 the shearing (plus extension) effect (cf. Eq. 4), in agreement with WKJ15 and other earlier  
 11 studies. However, since  $w$  and its horizontal gradient are weak near the surface, where the  
 12 vertical wind shear is larger (also Fig. 11c), the value of  $\nabla^2 p'_d$  is smaller than that in WKJ15.  
 13 Also, due to the farther distance, a direct role played by the dynamical pressure perturbations  
 14 in new cell initiation of B2 appears limited in the present case here.

15 Both B1 and B2 intensify at 21:00 UTC, and the latter, peaking at about  $1.5 \text{ m s}^{-1}$ , can now  
 16 reach 4 km while the layer of  $\nabla^2 p' > 0$  above (near 5 km) also grows stronger (Fig. 14j). A  
 17 downdraft at the rear flank of B1 reappears at mid-levels and penetrates down to 3 km at this  
 18 time, and acts to separate B2 from B1 (also Fig. 13d). Like earlier times since 20:20 UTC, the  
 19 total pattern of  $\nabla^2 p$  is dominated by  $\nabla^2 p'_b$  everywhere, except near the based of B1 (below  
 20 1.5 km) where  $\nabla^2 p'_d$  contributes significantly (Fig. 14k and l). Thus, the buoyancy-related  
 21 effect is consistently the more dominant one in the region of B2 during its initiation stage in  
 22 the model, suggesting the importance of near-surface convergence in driving the development  
 23 of the line-shaped MCS in this event, as also shown earlier in Sect. 4.2 (and cf. Fig. 11a).

24 Nevertheless, the propagation speed of B1 is indeed slower than B2 in Fig. 10, and can be  
 25 estimated to be about  $8.9 \text{ m s}^{-1}$  near 21:00 UTC. Caused by the dynamical effect of  $p'_d$ , this  
 26 slow down implies an increase in low-level blocking, and subsequent upstream convergence  
 27 by about  $1 \times 10^{-4} \text{ s}^{-1}$  using Fig. 11b (with a LLJ of  $12.5 \text{ m s}^{-1}$  near 40 km upstream), or  $2.2 \times$   
 28  $10^{-4} \text{ s}^{-1}$  larger than its surrounding with a background speed divergence of  $\sim 1.2 \times 10^{-4} \text{ s}^{-1}$   
 29 following WKJ15 (p.11109). Since this is no more than 20% of the maximum convergence  
 30 near B2 and its immediate upstream (west of  $121.2^\circ\text{E}$ , cf. Fig. 11a), the minor role of  $p'_d$  in  
 31 the initiation of B2 in the present case can be confirmed.



1 The buoyancy  $B$  (or more precisely, the vertical buoyant force per unit mass) in Eq. (1) and its  
 2 contributing terms as given in Eq. (2) on the same vertical cross-sections are shown in Fig. 15.  
 3 At 20:00 UTC, as expected,  $B$  is positive inside the cumulonimbus B1, and negative in the top  
 4 portion of the cloud ( $> 6.5$  km) and below the main updraft ( $< 2$  km, Fig. 15a). Such a pattern  
 5 is due to the combined effects of positive virtual potential temperature perturbation ( $\theta'_v > 0$ )  
 6 clearly from latent heat release (LHR) inside the cloud, and the downward drag by all  
 7 hydrometeors (including both cloud particles and precipitation) maximized below the updraft  
 8 core (Fig. 15b and c). In the downdrafts at the flanks (which originate from higher levels),  $B$   
 9 and  $g(\theta'_v/\theta_{v0})$  are also mostly positive from adiabatic warming outside the cloud.

10 From 20:20 to 21:00 UTC when the updraft of B1 becomes increasingly tilted, the buoyancy  
 11  $B$  in the core region of the updraft remains positive because of LHR, as the drag force shifts  
 12 toward the downwind side (Fig. 15d-l). Below and east of the updraft,  $B$  is strongly negative  
 13 near the surface due to the drag and a rapid reduction in positive  $\theta'_v$ , as the air descends. Even  
 14 though this reduction in  $\theta'_v$  suggests some evaporative cooling, the cold pool (and surface  
 15 outflow) would be to the east of B1, as confirmed in Fig. 12. On the upstream side where B2  
 16 is developing,  $B > 0$  appears near the surface with  $B < 0$  further aloft at 2-5 km (Fig. 15d, g,  
 17 and j) and can be attributed, respectively, to LHR and adiabatic cooling associated with  
 18 ascending motion (Fig. 15e, h, and k) in a convectively unstable environment. Apparently, as  
 19 B2 develops, the cooling above it and to the west (roughly 120.8-121°E) leads to a layer of  
 20 positive  $\partial B/\partial z$  and  $\nabla^2 p'_b$  near 5 km (cf. Eq. 3), since the air further above is stable (cf. Fig.  
 21 11a). In Fig. 15, however, one particular center of negative  $B$ , near 120.85°E and 3 km at  
 22 20:20 UTC, develops in a sinking area at the western edge of the cumulus, and therefore is  
 23 also enhanced by evaporative cooling of cloud droplets (Fig. 15d-l). Thus, the cooling and  
 24 subsequently  $B < 0$  (near 3 km) associated with B2 is not only by the adiabatic effect, but also  
 25 by evaporation at an earlier stage of initiation, for example, around 20:20 UTC (Fig. 15d and  
 26 e). However, at later times when the updraft of B1 becomes more tilted and B2 grows higher  
 27 and stronger, it becomes more difficult for the rear-flank downdraft to reach close to the  
 28 surface (cf. Fig. 15j-l), even though its strength can be sensitive to the cloud microphysical  
 29 scheme (e.g., Morrison et al., 2009).

30 Upstream from B1, the near-surface warming and cooling above, with maxima near 1 km and  
 31 3-4 km, respectively, create a decrease in buoyancy with height ( $\partial B/\partial z < 0$ ) that grows  
 32 stronger with time near B2 (Fig. 15d, g, and j). Together with the (near) exponential decrease

1 of  $\rho_0$  upward, this condition leads to  $\nabla^2 p'_b < 0$  in Eq. (3), and thus  $p'_b > 0$  that peaks slightly  
2 above 1 km and intensifies through time, as obtained using the relaxation method (Sect. 2.3)  
3 and shown in Fig. 16 (middle column). The upward decrease of  $p'_b$ , as the major component  
4 of total  $p'$ , in turn produces an upward-directed buoyant PGF to help B2 develop further (Fig.  
5 16, left and middle columns). Thus, the combined effect of buoyancy  $B$  (cf. Fig. 15, left  
6 column) and total perturbation PGF in the vertical [cf. Eq. (1)] is upward acceleration of  
7 parcels in B2 (Fig. 16, right column) to eventually reach free ascent and ignite deep  
8 convection (near 21:20 UTC, cf. Fig. 10).

9

## 10 **5 Discussion**

11 In the previous section, the pressure perturbation and buoyancy, dominated by the  
12 thermodynamic effects (including both adiabatic and diabatic ones from condensation or  
13 evaporation), as well as the resultant upward development at the initiation stage of cell B2 are  
14 examined (Figs. 13-16). The specific roles played by the old cell B1 in triggering B2,  
15 however, are still not fully clear. Therefore, we further compare the initiation of an isolated  
16 cell farther upstream, C1, where no existing cell is present nearby (cf. Figs. 9f and 10), with  
17 B1-B2 pair and discuss their differences. Obviously, cells like C1 can also develop on its own  
18 under the background forcing (cf. Fig. 9), as also seen in Fig. 6, but a comparison allows us to  
19 identify the additional role of B1 to new cell triggering, and thus to the BB process about 15-  
20 30 km upstream of the old cell in the present case.

21 Figure 17 shows similar plots as in Fig. 14, but through cell C1 on cross sections along the  
22 low-level convergence zone (WSW-ENE oriented) at 20:40 and 21:20 UTC, at the beginning  
23 of the initiation and right before the break out of deep convection, respectively (cf. Fig. 10).  
24 At 20:40 UTC (Fig. 17a), C1 is located near the left edge of the plots, while B2 appears near  
25 the right edge. At this early stage, the weak rising motion is associated with  $\nabla^2 p' > 0$  (or  $p' <$   
26  $0$ ) below about 1 km and  $\nabla^2 p' < 0$  (or  $p' > 0$ ) slightly above near 1-2.5 km, again mostly from  
27 the buoyant component (Fig. 17a-c). This pattern is because  $B$  is maximized near 1 km even  
28 though its value is negative ( $B < 0$ ) everywhere (not shown), indicating that the near-surface  
29 atmosphere is still stable and the positive  $w$  is forced by the convergence at this time.

30 At 21:20 UTC when C1 grows much stronger ( $\sim 1.5 \text{ m s}^{-1}$ ), the same pattern continues to  
31 amplify and extends upward, while  $p'_d$  remains to play little role without a mature cell (Fig.

1 17d-f). Now, with clouds reaching about 5 km,  $B$  has become positive at the core of C1  
2 (peaking over  $2 \times 10^{-3} \text{ m s}^{-2}$  near 1.5 km) due to LHR after saturation (Fig. 18a and b), giving  
3 a largest  $\theta'_v$  of  $\sim 1.2 \text{ K}$  (not shown). Near the cloud top and below the cloud base of C1, both  
4  $B$  and  $\theta'_v$  turn negative and can only come from adiabatic or evaporative cooling, or both. The  
5 cooling near 5-6 km explains the layer of  $\nabla^2 p'_b$  (and  $\nabla^2 p'$ )  $> 0$  immediately above (over 6-7  
6 km, Fig. 17d and e), as seen earlier in Fig. 14g and 14j above the developing B2 (near 5 km).  
7 The solutions of  $p'$  and  $p'_b$  by the relaxation method, linked to the pattern of their laplacian  
8 noted above, produce downward perturbation PGF (below  $\sim 2 \text{ km}$ , Fig. 18c and d) that  
9 partially cancels the upward buoyant force (cf. Fig. 18a).

10 Overall, the warming by LHR and the cooling above during the developing stage of new cells  
11 represent a destabilization in their low-level environment with time (Figs. 15 and 18). Forced  
12 by the background convergence (cf. Fig. 9), even though C1 eventually also develops into  
13 deep convection, the vertical perturbation PGF remains pointing down below about 2.5 km  
14 even at 21:20 UTC (Fig. 18c and d). On the contrary, it is positive above 1-1.5 km in B2 and  
15 helps its development at both 20:40 and 21:00 UTC (Fig. 16d and g). Consistent with this  
16 difference, in B2, the maximum center of  $p'_b$  occurs closer to the surface and it decreases with  
17 height more rapidly above, and three factors linked to the old cell B1 contribute to the  
18 establishment of the upward-directed perturbation PGF. First, a stronger cooling occurs near 3  
19 km above B2 (Fig. 15), at levels significantly lower than that above C1 (cf. Fig. 18), and this  
20 cooling is likely enhanced by evaporation of condensates near the western edge of B1  
21 (besides adiabatic effect). Second, a more rapid and efficient warming also occurs closer to  
22 the surface at the early stage of B2, and this is helped by the stronger LHR near the bottom of  
23 B1 (cf. Fig. 15). Both these effects can be thought of as a more rapid destabilization that gives  
24 the new cell the potential for a faster development. Finally, the separation by the descending  
25 branch of the old cell, when such a descent can reach a lower elevation, also plays a role in  
26 leading to BB process about 20 km upstream in the present case, based on our numerical  
27 simulation results in this case study. In C1 where  $B > 0$  is counteracted by a downward  
28 perturbation PGF, all three advantages are absent without a nearby old cell (Figs. 17 and 18).

29

## 30 **6 Conclusion and summary**

31 During 11-12 June 2012 in the mei-yu season, both TL/AS and BB MCSs developed in  
32 succession near northern Taiwan, and together produced extreme rainfall up to 510 mm

1 overnight in the Taipei metropolitan area, causing serious flooding in many densely-populated  
2 regions. Observations show that BB behavior occurred in these MCSs, especially in the  
3 second, E-W-aligned quasi-stationary linear MCS during 18:00-24:00 UTC 11 June (02:00-  
4 08:00 LST 12 June), and was a contributing factor to the extreme rainfall and related hazards  
5 in Taipei. The numerical simulation using the CReSS model with a horizontal grid size of 1.5  
6 km starting at 12:00 UTC 10 June successfully captured the development and evolution of the  
7 BB MCS (but with considerable position error for the preceding TL/AS system). In contrast  
8 to mid-latitude (and some subtropical) systems, the cold pool mechanism is not responsible  
9 for triggering new BB cells in the present MCS, and thus the model results are used to  
10 investigate the details of the BB process occurring specifically about 15-30 km upstream from  
11 old convective elements in this subtropical system.

12 In agreement with and supported by the observations, the linear BB MCS in the present event  
13 was forced by near-surface convergence ahead of the front, between the flow blocked and  
14 deflected northward (into southwesterly) by the topography of Taiwan and the unblocked  
15 (west-southwesterly) flow farther to the north and west in the environment. The approaching  
16 mei-yu front (about 80-30 km) to the north of the linear MCS, thus, helped provide and  
17 channel an enhanced prevailing flow to its south but did not play a direct role in the formation  
18 of the MCS. While the above processes all worked in synergy and contributed to the heavy  
19 rainfall, it is not possible to quantify their individual effect in the present study.

20 For the BB process at the convective scale, although the dynamic pressure perturbations ( $p'_d$ )  
21 from the interaction between the mature cells and the LLJ, with  $p'_d > 0$  ( $< 0$ ) at the rear  
22 (forward) flank of the updraft near the surface below the jet and a reversed pattern near 2-3  
23 km above the jet, can cause the mature cells to slow-down slightly and enhance the low-level  
24 convergence upstream, their effects are weaker compared to those found in WKJ15 for a case  
25 of typhoon rainband, and a direct role in new cell initiation appears quite limited.

26 In the present event, the total pressure perturbations ( $p'$ ) in the vicinity of the new cell  
27 throughout the initiation stage are attributed more to their buoyant ( $p'_b$ ) than dynamical  
28 component. Forced by the low-level convergence (parallel to the line) in the background, the  
29 early development of new cells, at convective scale, are associated with positive buoyancy ( $B$   
30  $> 0$ ) by latent heating below and negative buoyancy ( $B < 0$ ) by adiabatic cooling above, and  
31 this represents a gradual destabilization in their surrounding environment. By comparing the  
32 BB process with the initiation of an isolated cell, the additional and specific roles played by

1 the old cell to help trigger new convection to its west can be identified. At the initial stage, the  
2 development is close to the mature cell, which provides stronger warming below (and closer  
3 to the surface) and also additional cooling above from evaporation of condensates at its rear  
4 side. The more rapid upward decrease in  $B$  produces a positive  $p'_b$  at a lower height and  
5 subsequently an upward-directed perturbation (buoyant) PGF that drives further development  
6 together with the positive buoyancy. Thus, the net effect of the additional warming/cooling is  
7 essentially a more rapid destabilization that gives the new cell a faster development. After  
8 some time when the new cell has gained sufficient strength, a descending branch appearing at  
9 the rear flank of the old cell acts to separate the new cell to about 20 km upstream. The new  
10 cell continues to strengthen there, and eventually deep convection is ignited. Thus, the above  
11 roles played by the existing old cells, largely thermodynamic in origin but also helped by  
12 dynamical and kinematic effects, can explain why the spot roughly 15-30 km upstream from  
13 the western end of quasi-linear MCSs in the subtropics can often have advantages over other  
14 locations for new cell initiation in their back-building process, even in the absence of cold  
15 pool mechanism. To our knowledge, the above favorable factors that can be provided by the  
16 old cells in the BB MCSs, particularly not in association with the cold pool, have not been  
17 investigated in the literature before.

18

## 19 **Acknowledgements**

20 The authors wish to acknowledge the CWB and NCEP in providing the various data used in  
21 this study, and the helps from Mr. C.-Y. Lee in programming, and Mr. K.-Y. Chen and Ms.  
22 S.-Y. Huang in making some of the figures. This study is jointly supported by the Ministry of  
23 Science and Technology of Taiwan under Grants MOST-103-2119-M-003-001-MY2, MOST-  
24 103-2625-M-003-001-MY2, and MOST-105-2111-M-003-003-MY3.

25

## 26 **Appendix The relaxation method**

27 In this study, the relaxation method is used to numerically solve for the pressure perturbation  
28  $p$  from its 3-D laplacian  $\nabla^2 p$  ("prime" omitted for simplicity), where  $\nabla^2 p$  can be  $\nabla^2 p_b$ ,  $\nabla^2 p_d$ ,  
29 or any of the rhs terms in Eq. (3) or (4). In this appendix, its formulation and boundary  
30 conditions are described. Since the vertical grid spacing of CReSS is stretched, the values of  
31  $\nabla^2 p$  (and all other known variables in need) are first vertically interpolated to grid with a fixed

1  $\Delta z$  of 100 m, such that  $\Delta x = \Delta y = 1 \text{ km} = 10 \Delta z$ . At second-order accuracy, the 3-D laplacian  
 2 inside the calculation domain is approximated by the central-difference method as

$$3 \quad \nabla^2 p = \frac{p_{x+1} + p_{x-1} - 2p}{\Delta x^2} + \frac{p_{y+1} + p_{y-1} - 2p}{\Delta y^2} + \frac{p_{z+1} + p_{z-1} - 2p}{\Delta z^2} \quad (\text{A1})$$

4 where subscripts represent the  $p$  values of the next grid point on either side in each direction.  
 5 After rearranging terms to move only  $p$  (unknown) on the lhs and using  $\Delta x = \Delta y = 10 \Delta z$ , Eq.  
 6 (A1) can be rewritten as

$$7 \quad p = \frac{p_{x+1} + p_{x-1} + p_{y+1} + p_{y-1} + 10^2(p_{z+1} + p_{z-1}) - (\Delta x^2 \cdot \nabla^2 p)}{4 + 2 \times 10^2} \quad (\text{A2})$$

8 and used for interior grid points. On the boundary of the domain, the Neumann condition is  
 9 applied and the next grid point outside is assumed to have the same value as the one on the  
 10 boundary. For example,  $p_{x-1} = p$  on the western boundary, and the laplacian in  $x$ -direction  
 11 ( $\nabla^2 p_x$ ) in (A1) reduces to

$$12 \quad \nabla^2 p_x = \frac{p_{x+1} - p}{\Delta x^2} \quad (\text{A3})$$

13 while the two other rhs terms in  $y$  and  $z$  directions remain unchanged. So, on the western  
 14 boundary, the  $p_{x-1}$  term vanishes and the formula equivalent to Eq. (A2) becomes

$$15 \quad p = \frac{p_{x+1} + p_{y+1} + p_{y-1} + 10^2(p_{z+1} + p_{z-1}) - (\Delta x^2 \cdot \nabla^2 p)}{3 + 2 \times 10^2}. \quad (\text{A4})$$

16 Thus, on each of the remaining sides (and edges and corners) along the boundary of the 3-D  
 17 domain, the formula would take a different form from (A2) following a similar derivation.  
 18 Since the procedures are quite straight-forward, they are not repeated here.

19 Using equations including (A2) and (A4), the values of  $p$  can be numerically solved through  
 20 iteration. Starting from a set of first guess of  $p$ , all the terms on the RHS are known or can be  
 21 computed, and a new set of  $p$  on the LHS is obtained in each iteration going through all the  
 22 grid points. After each iteration, Eq. (A1) (or its equivalents on the boundaries) is used to  
 23 compute  $\nabla^2 p$  from the newly-obtained  $p$  and check against the true value (from Eqs. 3 or 4).  
 24 When the total absolute error of  $\nabla^2 p$  summed over all grid points reduces below the specified  
 25 threshold, the result converges and the iteration stops. Figures 13 and 15 of WKJ15 provide  
 26 some examples of the results obtained using the same relaxation method.

27

## 1 **References**

- 2 Bluestein, H. B., and Jain, M. H.: Formation of mesoscale lines of precipitation: severe squall  
3 lines in Oklahoma during the spring, *J. Atmos. Sci.*, 42, 1711-1732, 1985.
- 4 Brooks, H. E., and Stensrud, D. J.: Climatology of heavy rain events in the United States from  
5 hourly precipitation observations, *Mon. Weather Rev.*, 128, 1194-1201, 2000.
- 6 Browning, K. A.: Organization of clouds and precipitation in extratropical cyclones, in:  
7 *Extratropical Cyclones: The Erik Palmén Memorial Volume*, edited by: Newton, C. W. and  
8 Holopainen, E. O., Am. Meteor. Soc., Boston, MA, USA, 129-153, 1990.
- 9 Carbone, R. E.: A severe frontal rainband. Part I: Stormwide hydrodynamic structure, *J.*  
10 *Atmos. Sci.*, 39, 258-279, 1982.
- 11 Chappell, C. F.: Quasi-stationary convective events, in: *Mesoscale Meteorology and*  
12 *Forecasting*, edited by: Ray, P., Am. Meteor. Soc., Boston, MA, USA, 289-310, 1986.
- 13 Chen, G. T.-J.: Research on the phenomena of Meiyu during the past quarter century: An  
14 overview, *World Scientific Series for Meteorology of East Asia Volume 2. East Asian*  
15 *Monsoon*, edited by: Chang, C.-P. #et al., 357-403, 2004.
- 16 Chen, G. T.-J., and Chou, H.-C.: General characteristics of squall lines observed in TAMEX,  
17 *Mon. Weather Rev.*, 121, 726-733, 1993.
- 18 Chen, G. T.-J., and Yu, C.-C.: Study of low-level jet and extremely heavy rainfall over  
19 northern Taiwan in the mei-yu season. *Mon. Weather Rev.*, 116, 884-891, 1988.
- 20 Chen, G. T.-J., Wang, C.-C., and Liu, S. C.-S.: Potential vorticity diagnostics of a Mei-yu  
21 front case. *Mon. Weather Rev.*, 131, 2680-2696, 2003.
- 22 Chen, G. T.-J., Wang, C.-C., and Lin, D. T.-W.: Characteristics of low-level jets over  
23 northern Taiwan in Mei-yu season and their relationship to heavy rain events, *Mon.*  
24 *Weather Rev.*, 133, 20-43, 2005.
- 25 Corfidi, S. F.: Cold pools and MCS propagation: forecasting the motion of downwind-  
26 developing MCSs, *Weather Forecast.*, 18, 997-1017, 2003.
- 27 Corfidi, S. F., Meritt, J. H., and Fritsch, J. M.: Predicting the movement of mesoscale  
28 convective complexes, *Weather Forecast.*, 11, 41-46, 1996.

- 1 Cotton, W. R., Tripoli, G. J., Rauber, R. M., and Mulvihill, E. A.: Numerical simulation of the  
2 effects of varying ice crystal nucleation rates and aggregation processes on orographic  
3 snowfall, *J. Clim. Appl. Meteorol.*, 25, 1658-1680, 1986.
- 4 Ding, Y.: Summer monsoon rainfalls in China. *J. Meteor. Soc. Jpn.*, 70, 373-396, 1992.
- 5 Ding, Y., and Chan, J. C.-L. Chan: The East Asian summer monsoon: An overview. *Meteor.*  
6 *Atmos. Phys.*, 89, 117-142, 2005.
- 7 Doswell, C. A., III: Severe convective storms – an overview, in: *Severe Convective Storms*,  
8 *Meteor. Monogr.*, No. 50, Am. Meteor. Soc., Boston, MA, USA, ISBN: 978-1-878220-41-  
9 7, 1-26, 2001.
- 10 Doswell, C. A., III, Brooks, H. E., and Maddox, R. A.: Flash flood forecasting: an  
11 ingredients-based methodology, *Weather Forecast.*, 11, 560-581, 1996.
- 12 Figa-Saldaña, J., Wilson, J. J. W., Attema, E., Gelsthorpe, R., Drinkwater, M. R., and  
13 Stoffelen, A.: The Advanced Scatterometer (ASCAT) on the Meteorological Operational  
14 (MetOp) platform: A follow on for the European wind scatterometers, *Can. J. Remote*  
15 *Sens.*, 28, 404-412, 2002.
- 16 Fovell, R. G., Mullendore, G. L., and Kim, S.-H.: Discrete propagation in numerically  
17 simulated nocturnal squall lines, *Mon. Weather Rev.*, 134, 3735-3752, 2006.
- 18 Houston, A. L., and Wilhelmson, R. B.: Observational analysis of the 27 May 1997 central  
19 Texas tornadic event. Part I: Prestorm environment and storm maintenance/propagation,  
20 *Mon. Weather Rev.*, 135, 701-726, 2007.
- 21 Houze, R. A., Jr., Smull, B. F., and Dodge, P.: Mesoscale organization of springtime  
22 rainstorms in Oklahoma, *Mon. Weather. Rev.*, 118, 613-654, 1990.
- 23 Hsu, J.: ARMTS up and running in Taiwan, *Väisälä News*, 146, 24-26, 1998.
- 24 Ikawa, M., and Saito, K.: Description of a nonhydrostatic model developed at the Forecast  
25 Research Department of the MRI, MRI Tech. Rep. 28, Tsukuba, Japan, 238 pp, 1991.
- 26 James, R. P., and Markowski, P. M.: A numerical investigation of the effects of dry air aloft  
27 on deep convection, *Mon. Weather Rev.*, 138, 140-161, 2010.



- 1 Jeong, J.-H., Lee, D.-I., and Wang, C.-C.: A study on an extreme rainfall-producing quasi-  
2 stationary mesoscale convective system over southeastern Korea. Impact of cold pool,  
3 Mon. Weather Rev., revised, 2016.
- 4 Johnson, R. H., and Mapes, B. E.: Mesoscale processes and severe convective weather, in:  
5 Severe Convective Storms, edited by: Doswell, C. A., III, Meteor. Monogr., No. 50, Am.  
6 Meteor. Soc., Boston, MA, USA, ISBN: 978-1-878220-41-7, 71-122, 2001.
- 7 Jou, B. J.-D., and Deng, S.-M.: Structure of a low-level jet and its role in triggering and  
8 organizing moist convection over Taiwan: A TAMEX case study. Terr. Atmos. Oceanic  
9 Sci., 3, 39-58, 1992.
- 10 Klemp, J. B.: Dynamics of tornadic thunderstorms, Annu. Rev. Fluid Mech., 19, 369-402,  
11 1987.
- 12 Kondo, J.: Heat balance of the China Sea during the air mass transformation experiment, J.  
13 Meteor. Soc. Jpn., 54, 382-398, 1976.
- 14 Kuo, Y.-H., and Anthes, R. A.: Numerical simulation of a Mei-Yu system over southeastern  
15 Asia. Pap. Meteor. Res., 5, 15-36, 1982.
- 16 Kuo, Y.-H., and Chen, G. T.-J.: The Taiwan Area Mesoscale Experiment (TAMEX): An  
17 overview. Bull. Amer. Meteor. Soc., 71, 488-503, 1990.
- 18 LeMone, M. A., Zipser, E. J., and Trier, S. B.: The role of environmental shear and  
19 thermodynamic conditions in determining the structure and evolution of mesoscale  
20 convective systems during TOGA COARE, J. Atmos. Sci., 55, 3493-3518, 1998.
- 21 Li, J., and Chen, Y.-L.: Barrier jets during TAMEX, Mon. Weather Rev., 126, 959-971, 1998.
- 22 Li, J., Chen, Y.-L., and Lee, W.-C.: Analysis of a heavy rainfall event during TAMEX, Mon.  
23 Weather Rev., 125, 1060-1082, 1997.
- 24 Lin, Y.-L., Farley, R. D., and Orville, H. D.: Bulk parameterization of the snow field in a  
25 cloud model, J. Clim. Appl. Meteorol., 22, 1065-1092, 1983.
- 26 Louis, J. F., Tiedtke, M., and Geleyn, J. F.: A short history of the operational PBL –  
27 parameterization at ECMWF, in: Proceedings, ECMWF Workshop on Planetary Boundary  
28 Layer Parameterization, Reading, UK, 59-79, 1981.

- 1 Luo, Y., Gong, Y., and Zhang, D.-L.: Initiation and organizational modes of an extreme-rain-  
2 producing mesoscale convective system along a Mei-yu front in East China, *Mon. Weather*  
3 *Rev.*, 142, 203-221, 2014.
- 4 Morrison, H., Thompson, G., and Tatarskii, V.: Impact of cloud microphysics on the  
5 development of trailing stratiform precipitation in a simulated squall line: Comparison of  
6 one- and two-moment schemes, *Mon. Weather Rev.*, 137, 991-1007, 2009.
- 7 Maddox, R. A., Chappell, C. F., and Hoxit, L. R.: Synoptic and meso- $\alpha$  scale aspects of flash  
8 flood events, *Bull. Am. Meteor. Soc.*, 60, 115-123, 1979.
- 9 Meng, Z., Yan, D., and Zhang, Y.: General features of squall lines in East China, *Mon.*  
10 *Weather Rev.*, 141, 1629-1647, 2013.
- 11 Moore, B. J., Neiman, P. J., Ralph, F. M., and Barthold, F. E.: Physical processes associated  
12 with heavy flooding rainfall in Nashville, Tennessee, and vicinity during 1-2 May 2010:  
13 The role of an atmospheric river and mesoscale convective systems, *Mon. Weather Rev.*,  
14 140, 358-378, 2012.
- 15 Murakami, M.: Numerical modeling of dynamical and microphysical evolution of an isolated  
16 convective cloud---The 19 July 1981 CCOPE cloud, *J. Meteor. Soc. Jpn.*, 68, 107-128,  
17 1990.
- 18 Murakami, M., Clark, T. L., and Hall, W. D.: Numerical simulations of convective snow  
19 clouds over the Sea of Japan: two-dimensional simulation of mixed layer development and  
20 convective snow cloud formation, *J. Meteor. Soc. Jpn.*, 72, 43-62, 1994.
- 21 Parker, M. D., and Johnson, R. H.: Organizational modes of midlatitude mesoscale convective  
22 systems, *Mon. Weather Rev.*, 128, 3413-3436, 2000.
- 23 Parker, M. D., and Johnson, R. H.: Structures and dynamics of quasi-2D mesoscale  
24 convective systems, *J. Atmos. Sci.*, 61, 545-567, 2004.
- 25 Peters, J. M., and Roebber, P. J.: Synoptic control of heavy-rain-producing convective  
26 training episodes, *Mon. Weather Rev.*, 142, 2464-2482, 2014.
- 27 Peters, J. M., and Schumacher, R. S.: Mechanisms for organization and echo training in a  
28 flash-flood-producing mesoscale convective system, *Mon. Weather Rev.*, 143, 1058-1085,  
29 2015.

- 1 Rotunno, R., and Klemp, J. B.: The influence of the shear-induced pressure gradient on  
2 thunderstorm motion, *Mon. Weather Rev.*, 110, 136-151, 1982.
- 3 Rotunno, R., Klemp, J. B., and Weisman, M. L.: A theory for strong, long-lived squall lines, *J.*  
4 *Atmos. Sci.*, 45, 463-485, 1988.
- 5 Schumacher, R. S., and Johnson, R. H.: Organization and environmental properties of  
6 extreme-rain-producing mesoscale convective systems, *Mon. Weather Rev.*, 133, 961-976,  
7 2005.
- 8 Schumacher, R. S., and Johnson, R. H.: Characteristics of U.S. extreme rain events during  
9 1999-2003, *Weather Forecast.*, 21, 69-85, 2006.
- 10 Schumacher, R. S., and Johnson, R. H.: Quasi-stationary, extreme-rain-producing convective  
11 systems associated with midlevel cyclonic circulations, *Weather Forecast.*, 24, 555-574,  
12 2009.
- 13 Schumacher, R. S., Galarneau, T. J., Jr., and Bosart, L. F.: Distant effects of a recurving  
14 tropical cyclones on rainfall in a midlatitude convective system: A high-impact  
15 predecessor rain event. *Mon. Weather Rev.*, 139, 650-667, 2011.
- 16 Segami, A., Kurihara, K., Nakamura, H., Ueno, M., Takano, I., and Tatsumi, Y.: Operational  
17 mesoscale weather prediction with Japan Spectral Model, *J. Meteor. Soc. Jpn.*, 67, 907-924,  
18 1989.
- 19 Stevenson, S. N., and Schumacher, R. S.: A 10-year survey of extreme rainfall events in the  
20 central and eastern United States using gridded multisensor precipitation analyses, *Mon.*  
21 *Weather Rev.*, 142, 3147-3162, 2014.
- 22 Sun, J., and Lee, T.-Y.: A numerical study of an intense quasi-stationary convection band  
23 over the Korean Peninsula, *J. Meteor. Soc. Jpn.*, 80, 1221-1245, 2002.
- 24 Tompkins, A. M.: Organization of tropical convection in low vertical wind shears: The role of  
25 cold pools, *J. Atmos. Sci.*, 58, 1650-1672, 2001.
- 26 Tsuboki, K., and Sakakibara, A.: Large-scale parallel computing of cloud resolving storm  
27 simulator, in: *High Performance Computing*, edited by: Zima, H. P., Joe, K., Sato, M., Seo,  
28 Y., and Shimasaki, M., Springer-Verlag, Berlin and Heidelberg, Germany; New York, NY,  
29 USA, ISBN: 978-3-540-47847-8, 243-259, 2002.

- 1 Tsuboki, K., and Sakakibara, A.: Numerical Prediction of High-Impact Weather Systems: the  
2 Textbook for the Seventeenth IHP Training Course in 2007, Hydrospheric Atmospheric  
3 Research Center, Nagoya University and UNESCO, Nagoya, Japan, ISBN: 978-4-  
4 9980619-8-4, 273 pp, 2007.
- 5 Wang, C.-C.: The more rain, the better the model performs---The dependency of quantitative  
6 precipitation forecast skill on rainfall amount for typhoons in Taiwan, *Mon. Weather Rev.*,  
7 143, 1723-1748, 2015.
- 8 Wang, C.-C.: Paper of notes: The more rain from typhoons, the better the models perform.  
9 *Bull. Amer. Meteor. Soc.*, 97, 16-17, 2016.
- 10 Wang, C.-C., and Chen, G. T.-J.: Case study of the leeside mesolow and mesocyclone in  
11 TAMEX. *Mon. Weather Rev.*, 130, 2572-2592.
- 12 Wang, C.-C., and Huang, W.-M.: High-resolution simulation of a nocturnal narrow  
13 convective line off the southeastern coast of Taiwan in the mei-yu season, *Geophys. Res.*  
14 *Lett.*, 36, L06815, doi:10.1029/2008GL037147, 2009.
- 15 Wang, C.-C., Chen, G. T.-J., Chen, T.-C., and Tsuboki, K.: A numerical study on the effects  
16 of Taiwan topography on a convective line during the mei-yu season, *Mon. Weather Rev.*,  
17 133, 3217-3242, 2005.
- 18 Wang, C.-C., Chen, G. T.-J., and Huang, S.-Y.: Remote trigger of deep convection by cold  
19 outflow over the Taiwan Strait in the Mei-yu season: A modeling study of the 8 June 2007  
20 case, *Mon. Weather Rev.*, 139, 2854-2875, 2011.
- 21 Wang, C.-C., Kuo, H.-C., Chen, Y.-H., Huang, H.-L., Chung, C.-H., and Tsuboki, K.: Effects  
22 of asymmetric latent heating on typhoon movement crossing Taiwan: The case of Morakot  
23 (2009) with extreme rainfall, *J. Atmos. Sci.*, 69, 3172-3196, 2012.
- 24 Wang, C.-C., Kuo, H.-C., Yeh, T.-C., Chung, C.-H., Chen, Y.-H., Huang, S.-Y., Wang, Y.-W.,  
25 and Liu, C.-H.: High-resolution quantitative precipitation forecasts and simulations by the  
26 Cloud-Resolving Storm Simulator (CReSS) for Typhoon Morakot (2009), *J. Hydrol.*, 506,  
27 26-41, <http://dx.doi.org/10.1016/j.jhydrol.2013.02.018>, 2013.
- 28 Wang, C.-C., Hsu, J. C.-S., Chen, G. T.-J., and Lee, D.-I.: A study of two propagating heavy-  
29 rainfall episodes near Taiwan during SoWMEX/TiMREX IOP-8 in June 2008. Part I:

- 1 Synoptic evolution, episode propagation, and model control simulation, *Mon. Weather*  
2 *Rev.*, 142, 2619-2643, 2014a.
- 3 Wang, C.-C., Hsu, J. C.-S., Chen, G. T.-J., and Lee, D.-I.: A study of two propagating heavy-  
4 rainfall episodes near Taiwan during SoWMEX/TiMREX IOP-8 in June 2008. Part II:  
5 Sensitivity tests on the roles of synoptic conditions and topographic effects, *Mon. Weather*  
6 *Rev.*, 142, 2644-2664, 2014b.
- 7 Wang, C.-C., Kuo, H.-C., Johnson, R.-H., Lee, C.-Y., Huang, S.-Y., and Chen, Y.-H.: A  
8 numerical study of convection in rainbands of Typhoon Morakot (2009) with extreme  
9 rainfall: Roles of pressure perturbations with low-level wind maxima, *Atmos. Chem. Phys.*,  
10 15, 11097-11115, doi:10.5194/acp-15-11097-2015, 2015.
- 11 Wang, C.-C., Huang, S.-Y., Chen, S.-H., Chang, C.-S., and Tsuboki, K.: Cloud-resolving  
12 typhoon rainfall ensemble forecasts for Taiwan with large domain and extended range  
13 through time-lagged approach, *Weather Forecast.*, 31, 151-172, 2016a.
- 14 Wang, C.-C., Chen, G. T.-J., and Ho, K.-H.: A diagnostic case study of mei-yu frontal retreat  
15 and associated low development near Taiwan. *Mon. Weather Rev.*, 144, 2327-2349, 2016b.
- 16 Wang, H., Luo, Y.-L., and Jou, B. J.-D.: Initiation, maintenance, and properties of convection  
17 in an extreme rainfall event during SCMREX: observational analysis, *J. Geophys. Res.*  
18 *Atmos.*, 119: 13206-13232, doi: 10.1002/2014JD022339, 2014.
- 19 Weisman, M. L., and Klemp, J. B.: Characteristics of isolated convective storms, in:  
20 *Mesoscale Meteorology and Forecasting*, edited by: Ray, P. S., Am. Meteor. Soc., Boston,  
21 MA, USA, 331-358, 1986.
- 22 Weisman, M. L., and Rotunno, R.: "A theory for strong long-lived squall lines" revisited, *J.*  
23 *Atmos. Sci.*, 61, 361-382, 2004.
- 24 Wilhelmson, R. B., and Ogura, Y.: The pressure perturbation and the numerical modeling of a  
25 cloud, *J. Atmos. Sci.*, 29, 1295-1307, 1972.
- 26 Xu, W., Zipser, E. J., Chen, Y.-L., Liu, C., Liou, Y.-C., Lee, W.-C., and Jou, B. J.-D.: An  
27 orography-associated extreme rainfall event during TiMREX: Initiation, storm evolution,  
28 and maintenance, *Mon. Weather Rev.*, 140, 2555-2574, 2012.
- 29 Yang, M.-J., and Houze, R. A., Jr.: Multicell squall-line structure as a manifestation of  
30 vertically trapped gravity waves. *Mon. Weather Rev.*, 123, 641-661, 1995.

- 1 Yeh, H.-C., and Chen, Y.-L.: The role of offshore convergence on coastal rainfall during  
2 TAMEX IOP 3, *Mon. Weather Rev.*, 130, 2709-2730, 2002.
- 3 Yu, C.-K., and Chen, Y.: Surface fluctuations associated with tropical cyclone rainbands  
4 observed near Taiwan during 2000-08, *J. Atmos. Sci.*, 68, 1568-1585, 2011.
- 5 Zhang, M., and Zhang, D.-L.: Subkilometer simulation of a torrential-rain-producing  
6 mesoscale convective system in East China. Part I: Model verification and convective  
7 organization, *Mon. Weather Rev.*, 140, 184-201, 2012.
- 8

1 Table 1. The CReSS model domain configuration and physics used in this study.

2

Projection	Lambert Conformal (center at 120°E, secant at 10°N and 40°N)
Grid spacing	1.5 km × 1.5 km × 100-980 m (400 m)*
Dimension and size ( <i>x, y, z</i> )	1000 × 800 × 50 (1500 km × 1200 km × 20 km)
IC/BCs	NCEP 0.5° × 0.5° analyses (26 levels, every 6 h)
Topography and SST	Real at (1/120)° and weekly mean on 1° × 1° grid
Integration period	1200 UTC 10 Jun to 1200 UTC 12 Jun 2012 (48 h)
Output frequency	Every 15 min (every 5 min during 1800-2400 UTC 11 Jun)
Cloud microphysics	Bulk cold-rain scheme (6 species)
PBL parameterization	1.5-order closure with prediction of turbulent kinetic energy
Surface processes	Energy/momentum fluxes, shortwave and longwave radiation
Substrate soil model	41 levels, every 5 cm to 2m deep

3 \* The vertical grid spacing ( $\Delta z$ ) of CReSS is stretched (smallest at the bottom), and the  
4 averaged spacing is given in the parentheses.

5

## 1 **Figure captions**

2 Figure 1. CWB surface analyses and positions of front/trough (or wind-shift line, thick dashed)  
3 at 850 (red), 700 (blue), 500 (green), and 200 hPa (orange) at 12:00 UTC 11 Jun 2012. The  
4 CReSS model domain is marked by the dotted box.

5 Figure 2. (a) NCEP ( $0.5^\circ$ ) 950 hPa analysis and (b) CReSS simulation of horizontal winds ( $m$   
6  $s^{-1}$ , speed shaded, scale to the right) at  $z = 549$  m at 12:00 UTC 11 Jun 2012, with frontal  
7 position marked (thick dashed lines). (c, d) Frontal positions every 6 h from 06:00 UTC 11  
8 Jun to 12:00 UTC 12 Jun 2012 (c) at 950 hPa in NCEP analyses and (d) at  $z = 549$  m in model  
9 (see legend for line color and style), overlaid with topography (km, shading, scale to the right).  
10 The triangle in (c) marks the location of Panchiao sounding in Fig. 3. (e, f) ASCAT oceanic  
11 winds ( $m s^{-1}$ ) near Taiwan at (e) 13:00 UTC 11 Jun and (f) 02:00 UTC 12 Jun, 2012, with  
12 surface frontal position analyzed.

13 Figure 3. Thermodynamic (skew  $T$ -log  $p$ ) diagram for the sounding taken at Panchiao (46692,  
14 cf. Fig. 2c for location) at 12:00 UTC 11 Jun 2012. For winds, full (half) barbs denote 10 (5)  
15 kts ( $1 \text{ kt} = 0.5144 \text{ m s}^{-1}$ ), respectively.

16 Figure 4. Composite VMI radar reflectivity (dBZ, color, scale to the right) over the Taiwan  
17 area at 1 h intervals from (a) 12:00 UTC 11 Jun to (i) 02:00 UTC 12 Jun, 2012. The outline of  
18 Taiwan is highlighted (thick dotted lines) and the surface frontal position is plotted at synoptic  
19 times (thick dashed lines).

20 Figure 5. Distribution of observed 6-h accumulated rainfall (mm, color, scale to the right)  
21 over Taiwan during (a) 12:00-18:00 UTC and (b) 18:00-24:00 UTC 11 Jun 2012. The Taipei  
22 City boundary is depicted in panel (a), and the dotted box in (b) shows the region used in Fig.  
23 8 for rainfall average. (c, d) As in (a, b), but showing model-simulated rainfall over Taiwan  
24 and the surrounding oceans.

25 Figure 6. As in Fig. 4, but showing reflectivity over northern Taiwan and the upstream area  
26 every 10 min from (a) 19:40 UTC to (o) 22:00 UTC 11 Jun 2012 using a different set of  
27 colors. The arrows mark the initiation or strengthening of back-building cells, off the western  
28 end of a rainband or upstream from an old cell.

29 Figure 7. CReSS simulation of surface winds at 10 m height ( $m s^{-1}$ ) and column-maximum  
30 mixing ratio of precipitation (rain + snow + graupel,  $g \text{ kg}^{-1}$ , shading, scale to the right) every



1 2 h from (a) 12:00 UTC to (f) 22:00 UTC 11 Jun 2012. For winds, full (half) barbs denote 10  
2  $(5) \text{ m s}^{-1}$ , and the surface frontal positions are marked (thick dashed lines). The rectangle in  
3 panel (a) depicts the area  $(24.75\text{-}25.15^\circ\text{N}, 120.35\text{-}121.75^\circ\text{E})$  used for the separation method.

4 Figure 8. Time series of observed (gray bars) and simulated (curve with dots) hourly rainfall  
5 (mm), averaged inside the box shown in Fig. 5b  $(24.75\text{-}25.17^\circ\text{N}, 120.87\text{-}121.85^\circ\text{E})$  over  
6 northern Taiwan from 12:00 UTC 11 Jun to 06:00 UTC 12 Jun 2012.

7 Figure 9. CReSS simulation of horizontal winds ( $\text{m s}^{-1}$ , vectors, reference length at bottom)  
8 and convergence/divergence ( $10^{-4} \text{ s}^{-1}$ , shading, scale to the right, positive for convergence) at  
9 312-m height (contoured in thick gray) every 30 min from (a) 18:30 UTC to (f) 21:00 UTC 11  
10 Jun 2012. The frontal positions (black dotted lines), and convergence axis (green dotted lines)  
11 and convective cells of interests are marked.

12 Figure 10. Model-simulated column-maximum vertical velocity ( $w$ ,  $\text{m s}^{-1}$ , color and thin  
13 contours) every 10 min during 19:20-22:10 UTC 11 Jun 2012, overlaid with terrain elevation  
14 (m, thick contours at 250 and 500 m) in northern Taiwan. The color scale is shown at the  
15 bottom, and the contour at  $0.5 \text{ m s}^{-1}$  is not drawn. Old cells (A1, B1, and C1) and nearby new  
16 cells (A2, B2) of interests are labeled. Green dashed lines AB and CD depict the vertical  
17 cross-sections used in Fig. 11, and the short segments depict those used in Figs. 14-18 (blue  
18 (brown) ones through B1 (C1)).

19 Figure 11. (a) E-W vertical cross-section of model-simulated convergence/divergence ( $10^{-4}$   
20  $\text{s}^{-1}$ , color, positive for convergence) and  $\theta_e$  (K, contour, every 1 K) along  $25^\circ\text{N}$  (line AB in  
21 Fig. 10), averaged over 21:25-21:35 UTC 11 Jun 2012. The triangle marks the mean location  
22 of the updraft of B1. (b, c) As in panel (a), except showing (b) convergence/divergence (color)  
23 and wind vectors ( $\text{m s}^{-1}$ ) and speed (isotach every  $1 \text{ m s}^{-1}$ ) and (c)  $w$  ( $\text{m s}^{-1}$ , color) and  
24 vertical wind shear vector ( $10^{-3} \text{ s}^{-1}$ , in cardinal direction, reference vectors both plotted)  
25 along the WSW-ENE section (line CD in Fig. 10) at 21:00 UTC 11 Jun 2012. Thick arrow-  
26 lines in (b, c) depict the axis of the LLJ.

27 Figure 12. CReSS simulation of convergence/divergence ( $10^{-4} \text{ s}^{-1}$ , shading, scale to the right,  
28 positive for convergence), 10-m wind perturbation ( $\text{m s}^{-1}$ , green vectors, reference length at  
29 bottom), and potential temperature perturbation ( $\theta'$ , K, contours every 0.1 K, dashed for  
30 negative values) at the surface every 20 min from (a) 20:00 UTC to (f) 21:00 UTC 11 Jun  
31 2012. Cells B1 (black) and B2 (blue), axis of convergence (thick dotted line) produced by

1 downdraft outflow of B1, and locations of vertical cross sections as in Fig. 10 (straight dashed  
2 lines) are marked.

3 Figure 13. Model-simulated  $w$  ( $\text{m s}^{-1}$ , color, scale at bottom) and laplacian of perturbation  
4 pressure ( $10^{-6} \text{ Pa m}^{-2}$ , contour, every  $3 \times 10^{-6} \text{ Pa m}^{-2}$ , dashed for negative values) of cells B1  
5 and B2 at (left) 806 m and (right) 2929 m at 21:00 UTC 11 Jun 2012. (a, d)  $\nabla^2 p'$  obtained  
6 from separation method, and (b, e)  $\nabla^2 p' = \nabla^2 p'_b + \nabla^2 p'_d$  and (c, f)  $\nabla^2 p'_b$  computed from Eqs.  
7 (3) and (4). Cells B1 and B2 and updraft and downdraft centers are labeled in panels (a) and  
8 (d).

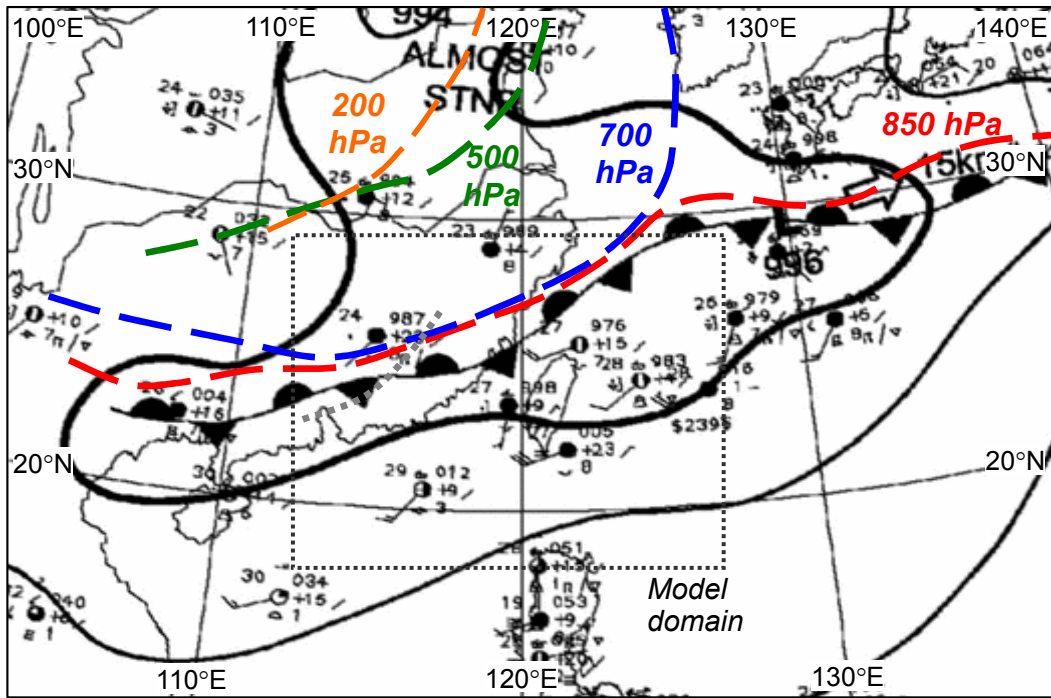
9 Figure 14. Vertical cross-sections of model-simulated  $w$  ( $\text{m s}^{-1}$ , color) and (a)  $\nabla^2 p'$  ( $10^{-6} \text{ Pa}$   
10  $\text{m}^{-2}$ ) and wind vectors ( $\text{m s}^{-1}$ , reference vector at bottom) on section plain, (b)  $\nabla^2 p'_b$   
11 (computed from Eq. 3), and (c)  $\nabla^2 p'_d$  (computed from Eq. 4) and vertical wind shear vector  
12 ( $10^{-3} \text{ s}^{-1}$ , in cardinal direction, reference vector at bottom) along the E-W segment through B1  
13 and B2 at 20:00 UTC 11 Jun 2012 (cf. Fig. 10). All contour intervals are  $3 \times 10^{-6} \text{ Pa m}^{-2}$   
14 (zero line omitted, dashed for negative values), and letters H (L) denote corresponding high  
15 (low) pressure perturbations. (d-f), (g-i), and (j-l) As in (a-c), except at 20:20, 20:40, 21:00  
16 UTC (WNW-ESE segments for 20:40 and 21:00 UTC, cf. Fig. 10), respectively.

17 Figure 15. (a-c) As in Fig. 14a-c, but showing  $w$  and (a) buoyancy  $B$  ( $10^{-3} \text{ m s}^{-2}$ , black  
18 contour) and mixing ratio of cloud particles ( $\text{g kg}^{-1}$ , blue contour, every  $3 \text{ g kg}^{-1}$ ), (b)  
19  $g(\theta'_v/\theta_{v0})(10^{-3} \text{ m s}^{-2})$ , and (c)  $-g\sum q_x$  ( $10^{-3} \text{ m s}^{-2}$ ). All black contour intervals are  $3 \times 10^{-6} \text{ Pa}$   
20  $\text{m}^{-2}$  (dashed for negative values, zero line omitted), and + (–) signs denote upward  
21 (downward) maxima. (d-f), (g-i), and (j-l) As in (a-c), except at 20:20, 20:40, and 21:00 UTC,  
22 respectively.

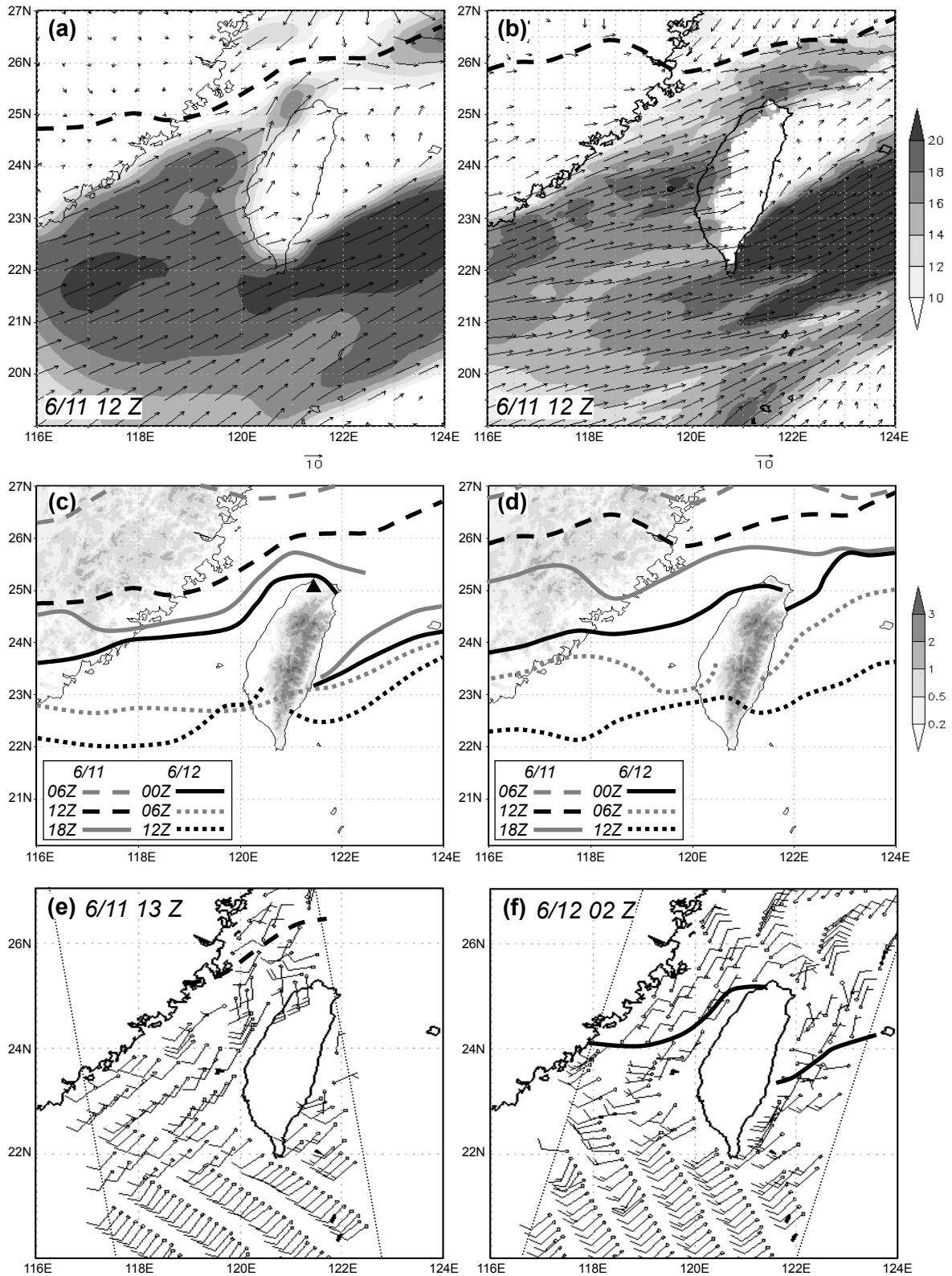
23 Figure 16. As in Fig. 14, but showing  $w$  and (a, d, g)  $p' = p'_b + p'_d$  (Pa, black contour, every  
24 10 Pa, dashed for negative values) obtained from the relaxation method and the corresponding  
25 perturbation PGF in the vertical ( $-(\partial p'/\partial z)/\rho_0$ ,  $10^{-3} \text{ m s}^{-2}$ , blue contour), (b, e, h)  $p'_b$  (Pa) and  
26 its vertical PGF ( $10^{-3} \text{ m s}^{-2}$ ), and (c, f, i)  $dw/dt$  from vertical perturbation PGF and  $B$  ( $10^{-3} \text{ m}$   
27  $\text{s}^{-2}$ , black contour). For force (per unit mass) and acceleration, all contour intervals are  $5 \times$   
28  $10^{-3} \text{ m s}^{-2}$  (dashed for negative values), and upward (downward) arrows denote maxima  
29 (minima).

1 Figure 17. As in Fig. 14, but showing  $w$  ( $\text{m s}^{-1}$ , color) and (a)  $\nabla^2 p'$  ( $10^{-6} \text{ Pa m}^{-2}$ ) and wind  
2 vectors ( $\text{m s}^{-1}$ ) on section plain, (b)  $\nabla^2 p'_b$ , and (c)  $\nabla^2 p'_d$  and vertical wind shear vector ( $10^{-3}$   
3  $\text{s}^{-1}$ , in cardinal direction) along the WSW-ENE segment through C1 at 20:40 UTC 11 Jun  
4 2012 (cf. Fig. 10). (d-f) As in (a-c), except at 21:20 UTC.

5 Figure 18. (a, b) As in Fig. 15a and b, but showing  $w$  (color) and (a)  $B$  (black contour) and  
6 mixing ratio of cloud particles (blue contour) and (b)  $g(\theta'_v/\theta_{v0})$  along the WSW-ENE segment  
7 through C1 at 21:20 UTC 11 Jun 2012. (c, d) As in Fig. 16a and b, but showing  $w$  and (c)  $p'$   
8 (black contour) obtain from the relaxation method and  $-(\partial p'/\partial z)/\rho_0$  (blue contour) and (d)  $p'_b$   
9 and its vertical PGF along the segment as in panels (a, b) at 21:20 UTC.

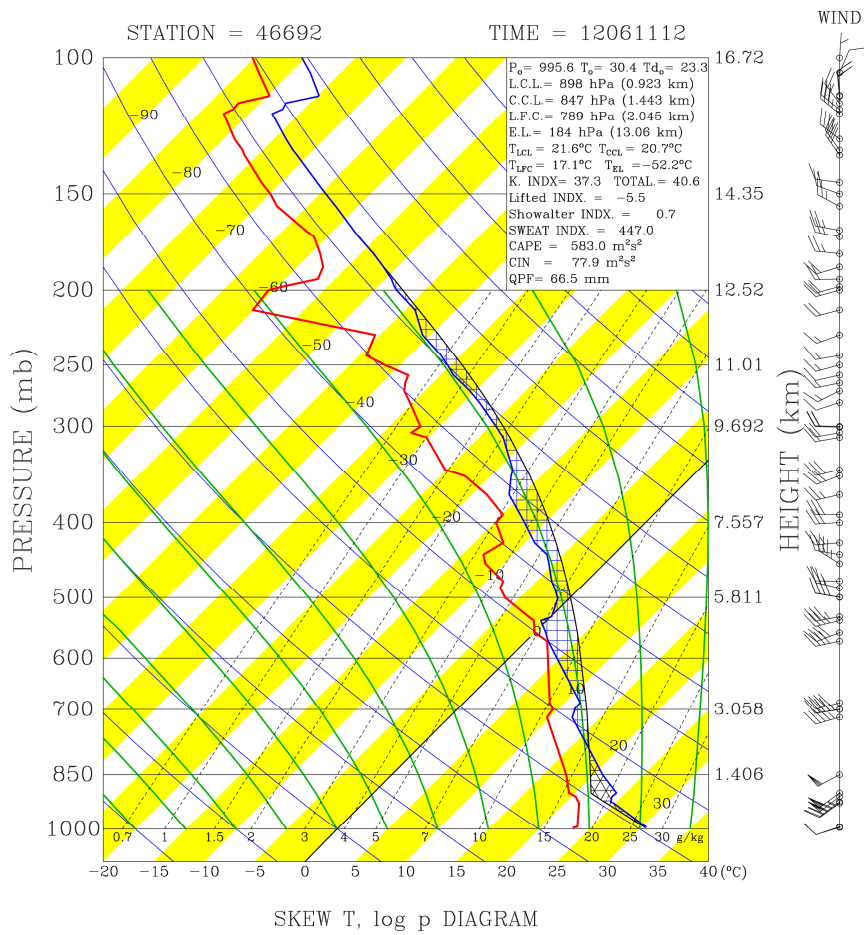


1 Figure 1. CWB surface analyses and positions of front/trough (or wind-shift line, thick dashed)  
 2 at 850 (red), 700 (blue), 500 (green), and 200 hPa (orange) at 12:00 UTC 11 Jun 2012. The  
 3 CReSS model domain is marked by the dotted box.

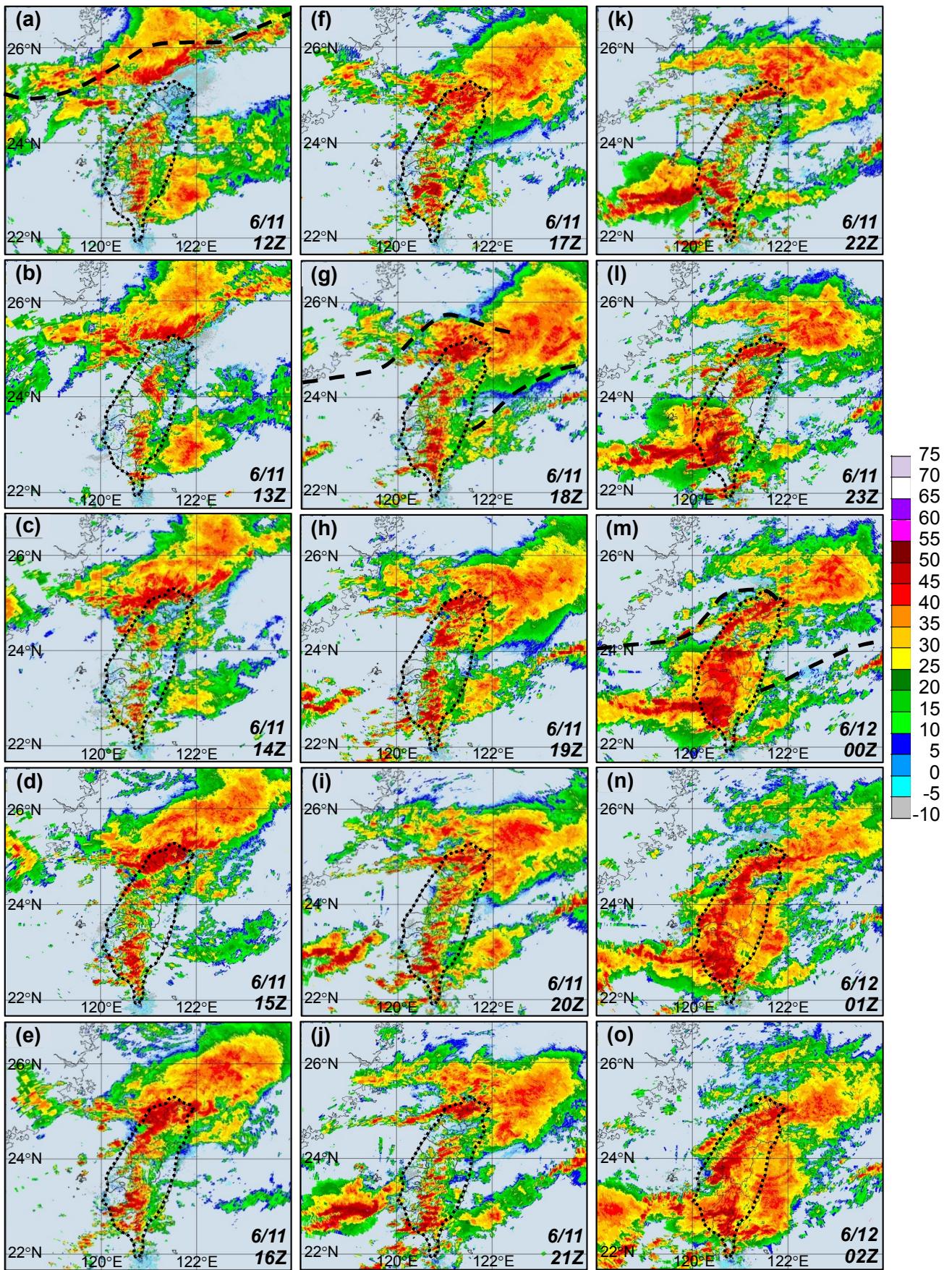


1 Figure 2. (a) NCEP (0.5°) 950 hPa analysis and (b) CReSS simulation of horizontal winds (m  
 2  $\text{s}^{-1}$ , speed shaded, scale to the right) at  $z = 549$  m at 12:00 UTC 11 Jun 2012, with frontal  
 3 position marked (thick dashed lines). (c, d) Frontal positions every 6 h from 06:00 UTC 11

1 Jun to 12:00 UTC 12 Jun 2012 (c) at 950 hPa in NCEP analyses and (d) at  $z = 549$  m in model  
2 (see legend for line color and style), overlaid with topography (km, shading, scale to the right).  
3 The triangle in (c) marks the location of Panchiao sounding in Fig. 3. (e, f) ASCAT oceanic  
4 winds ( $\text{m s}^{-1}$ ) near Taiwan at (e) 13:00 UTC 11 Jun and (f) 02:00 UTC 12 Jun, 2012, with  
5 surface frontal position analyzed.

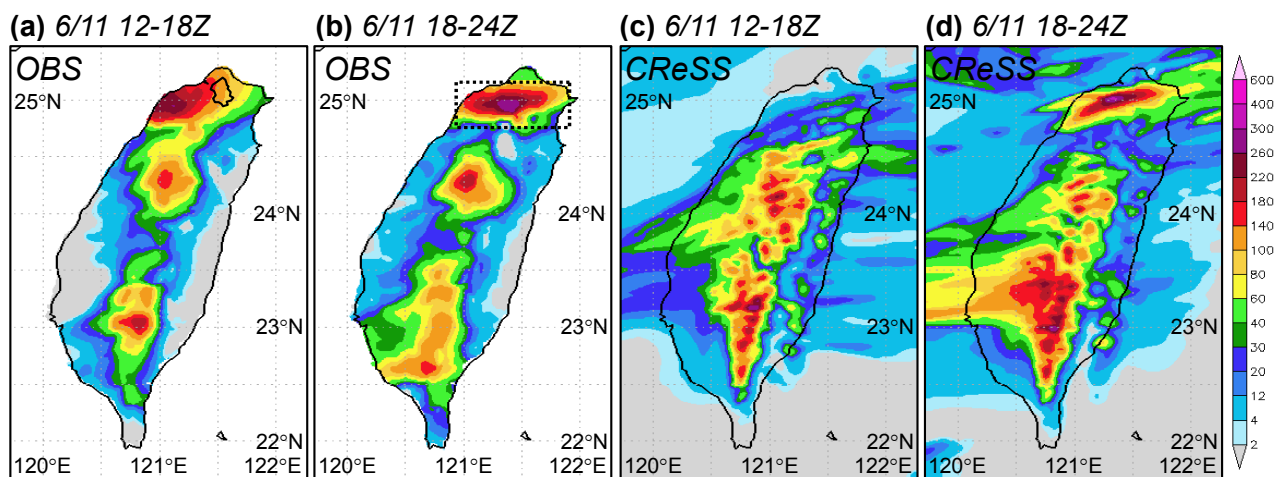


1 Figure 3. Thermodynamic (skew  $T$ -log  $p$ ) diagram for the sounding taken at Panchiao (46692,  
 2 cf. Fig. 2c for location) at 12:00 UTC 11 Jun 2012. For winds, full (half) barbs denote 10 (5)  
 3 kts (1 kt = 0.5144  $m s^{-1}$ ), respectively.

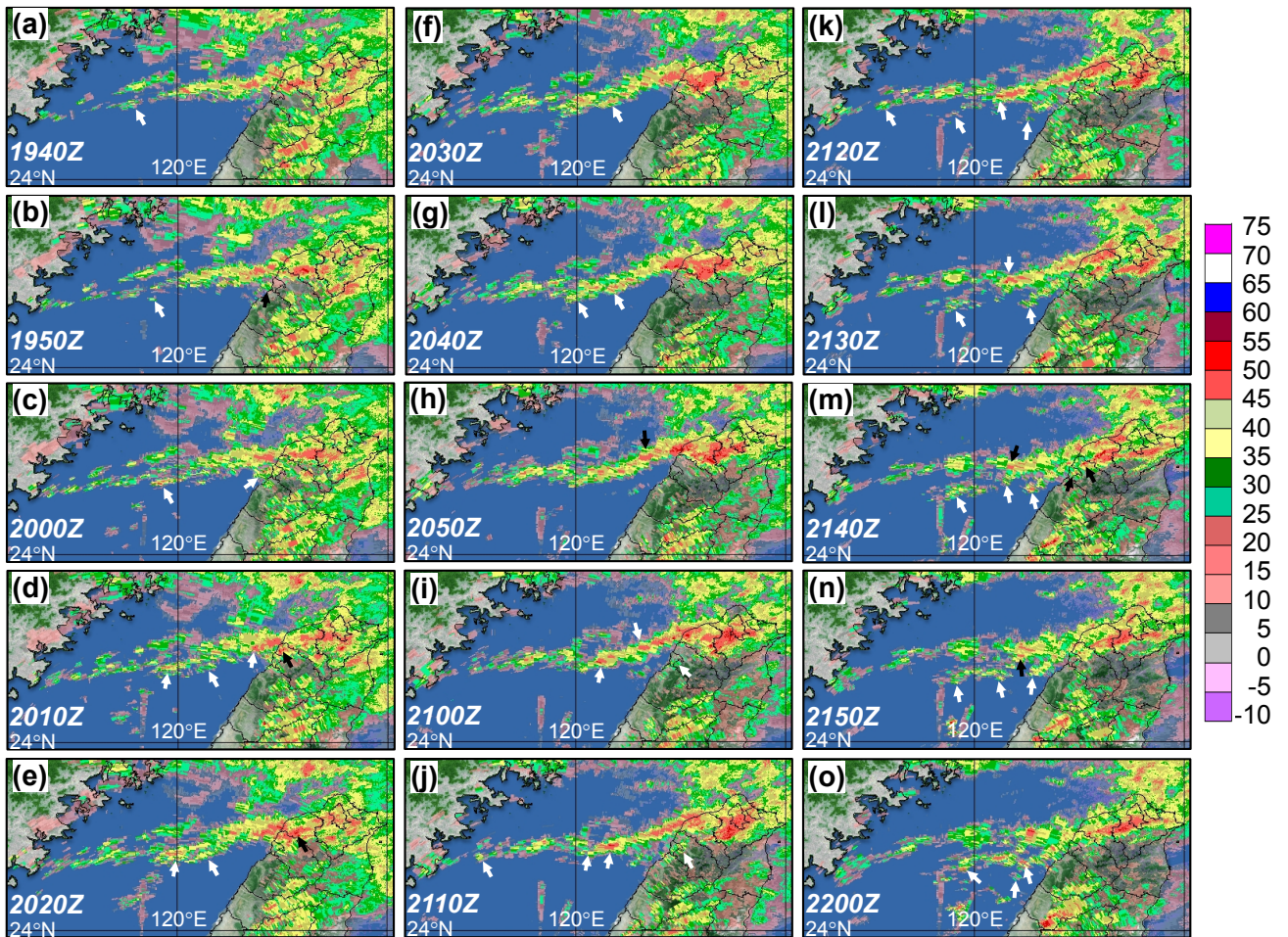




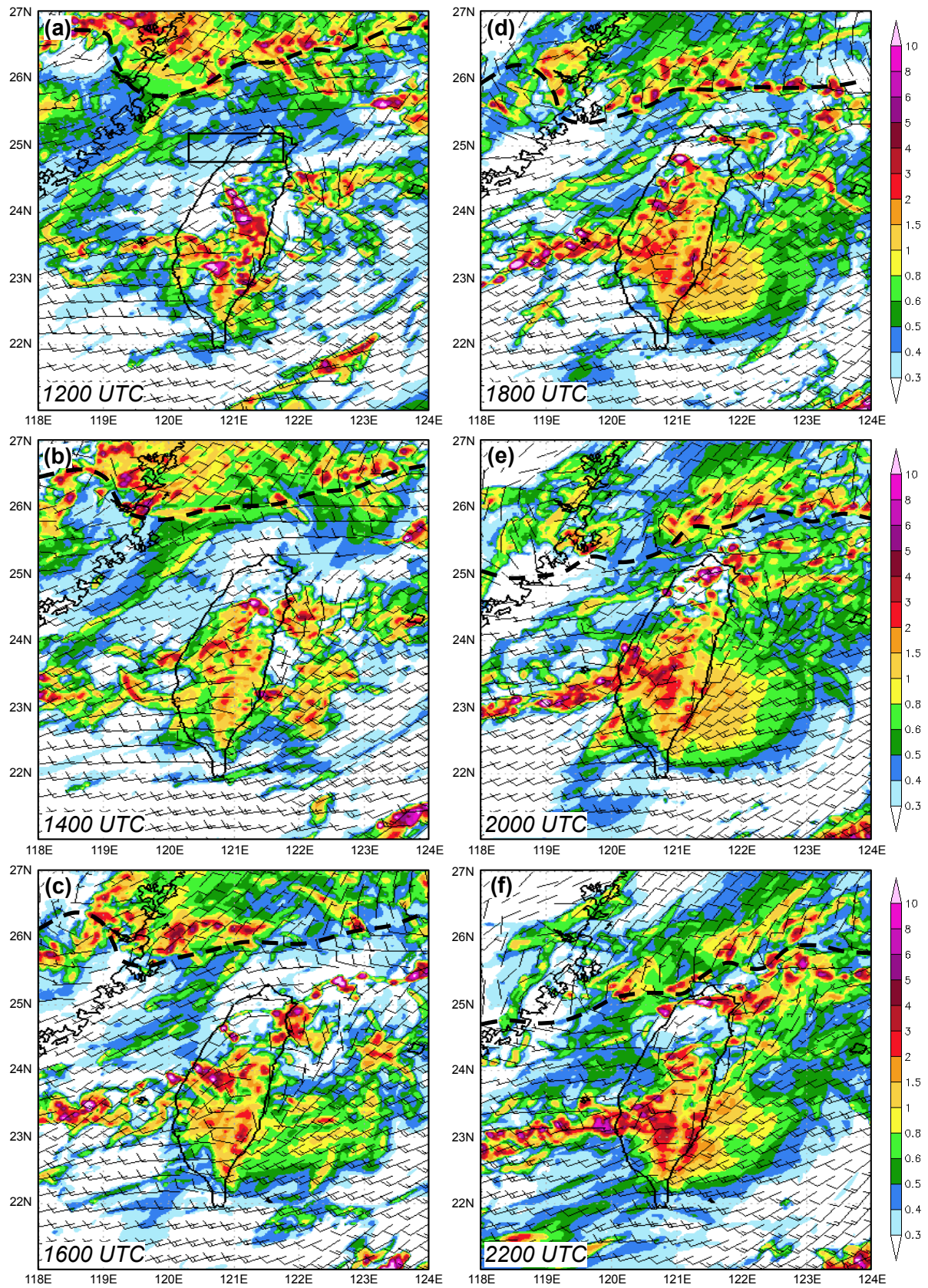
1 Figure 4. Composite VMI radar reflectivity (dBZ, color, scale to the right) over the Taiwan  
2 area at 1-h intervals from (a) 1200 UTC 11 Jun to (i) 0200 UTC 12 Jun, 2012. The outline of  
3 Taiwan is highlighted (thick dotted lines) and the surface frontal position is plotted at synoptic  
4 times (thick dashed lines).



1 Figure 5. Distribution of observed 6-h accumulated rainfall (mm, color, scale to the right)  
 2 over Taiwan during (a) 12:00-18:00 UTC and (b) 18:00-24:00 UTC 11 Jun 2012. The Taipei  
 3 City boundary is depicted in panel (a), and the dotted box in (b) shows the region used in Fig.  
 4 9 for rainfall average. (c, d) As in (a, b), but showing model-simulated rainfall over Taiwan  
 5 and the surrounding oceans.

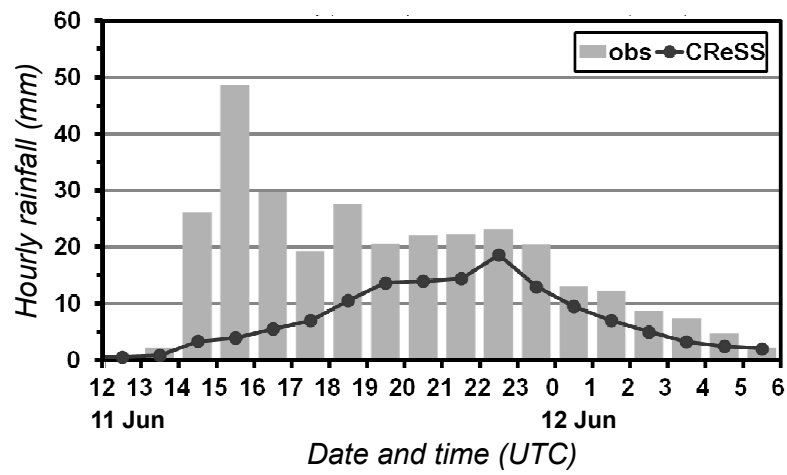


1 Figure 6. As in Fig. 4, but showing reflectivity over northern Taiwan and the upstream area  
 2 every 10 min from (a) 19:40 UTC to (o) 22:00 UTC 11 Jun 2012 using a different set of  
 3 colors. The arrows mark the initiation or strengthening of back-building cells, off the western  
 4 end of a rainband or upstream from an old cell.

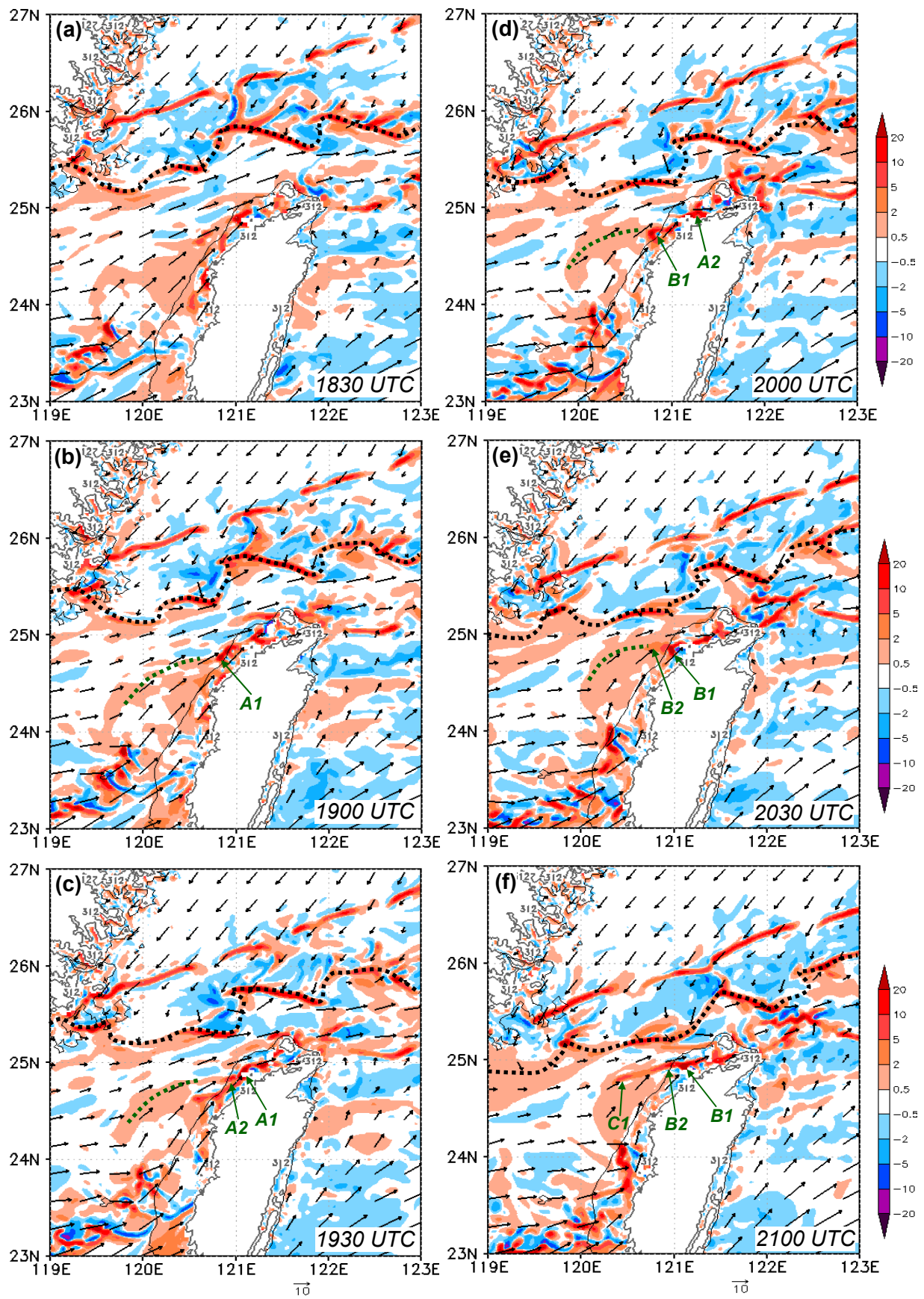


1 Figure 7. CReSS simulation of surface winds at 10 m height ( $\text{m s}^{-1}$ ) and column-maximum  
 2 mixing ratio of precipitation (rain + snow + graupel,  $\text{g kg}^{-1}$ , shading, scale to the right) every

1 2 h from (a) 12:00 UTC to (f) 22:00 UTC 11 Jun 2012. For winds, full (half) barbs denote 10  
2 (5)  $\text{m s}^{-1}$ , and the surface frontal positions are marked (thick dashed lines). The rectangle in  
3 panel (a) depicts the area (24.75-25.15°N, 120.35-121.75°E) used for the separation method.



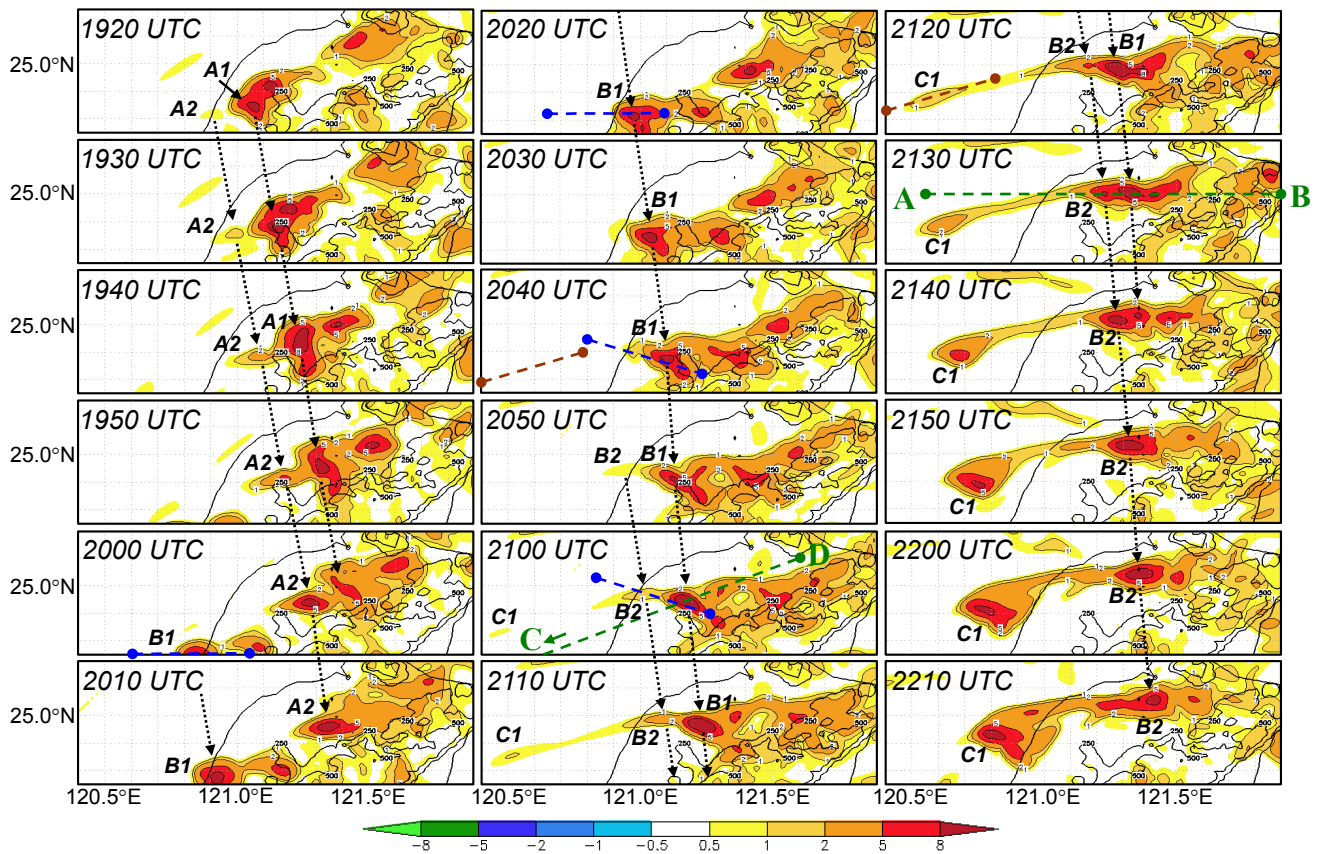
1 Figure 8. Time series of observed (gray bars) and simulated (curve with dots) hourly rainfall  
 2 (mm), averaged inside the box shown in Fig. 5b (24.75-25.17°N, 120.87-121.85°E) over  
 3 northern Taiwan from 12:00 UTC 11 Jun to 06:00 UTC 12 Jun 2012.



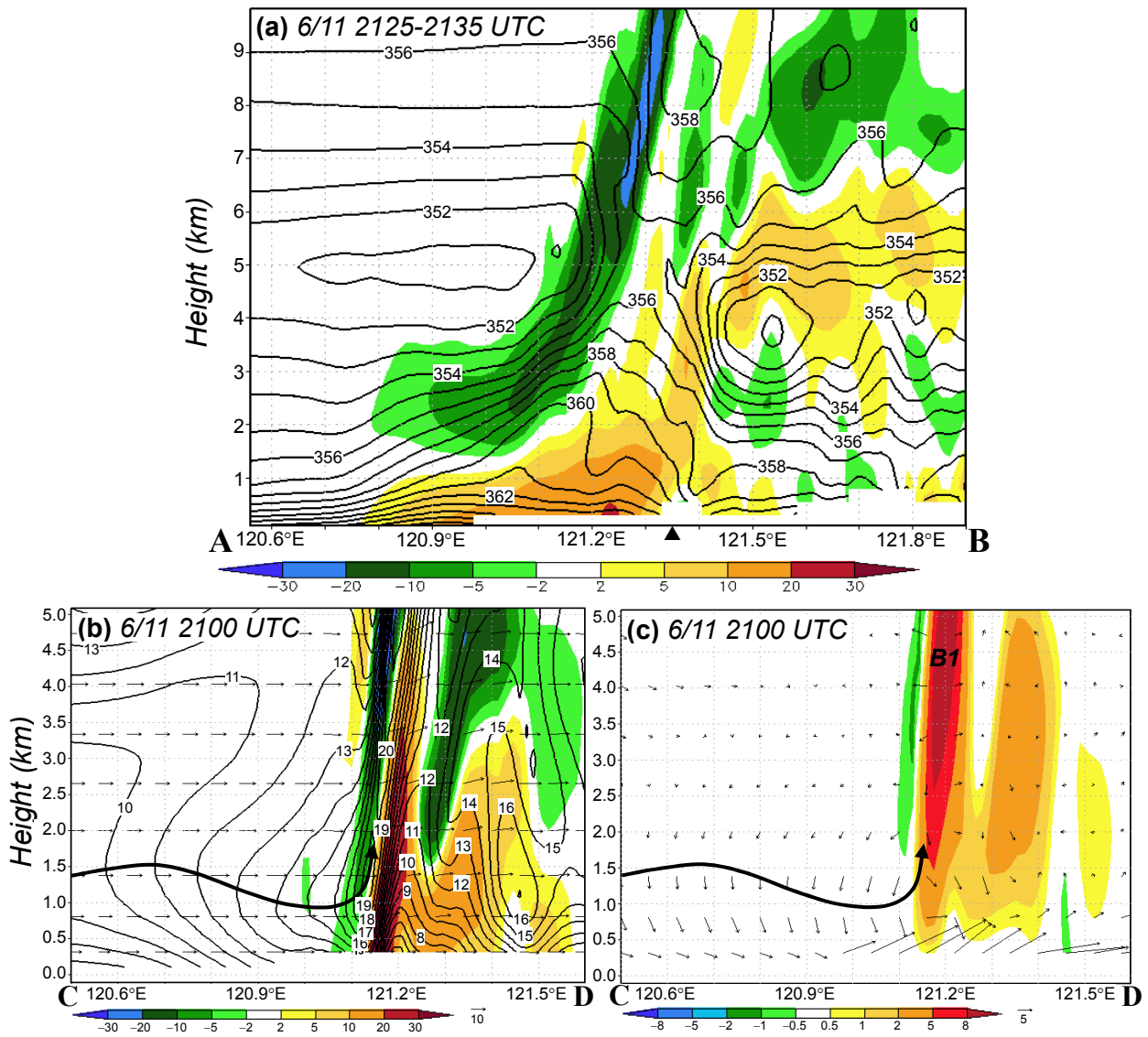
1 Figure 9. CReSS simulation of horizontal winds ( $\text{m s}^{-1}$ , vectors, reference length at bottom)

- 1 and convergence/divergence ( $10^{-4} \text{ s}^{-1}$ , shading, scale to the right, positive for convergence) at
- 2 312-m height (contoured in thick gray) every 30 min from (a) 18:30 UTC to (f) 21:00 UTC 11
- 3 Jun 2012. The frontal positions (black dotted lines), and convergence axis (green dotted lines)
- 4 and convective cells of interests are marked.

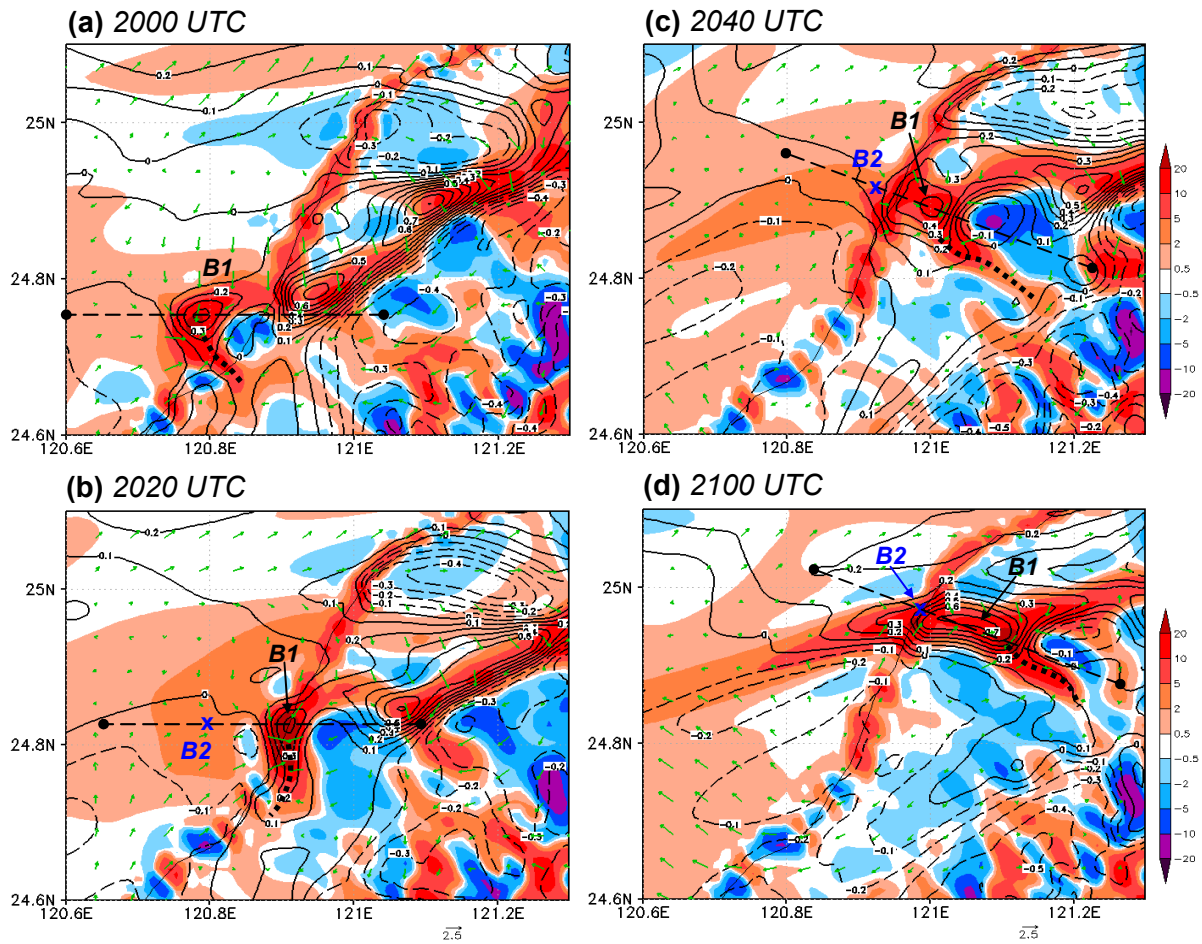




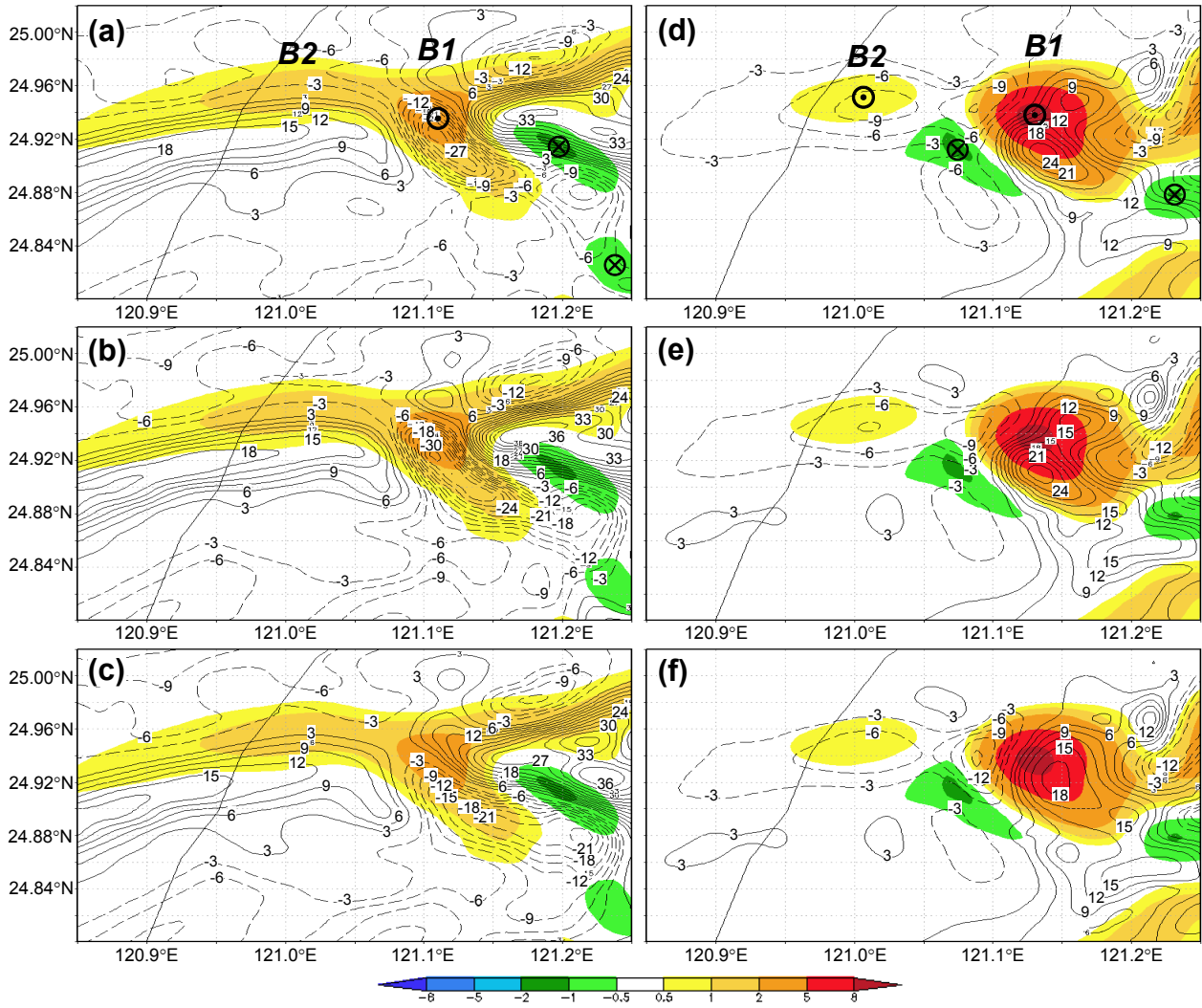
1 Figure 10. Model-simulated column-maximum vertical velocity ( $w$ ,  $\text{m s}^{-1}$ , color and thin  
 2 contours) every 10 min during 19:20-22:10 UTC 11 Jun 2012, overlaid with terrain elevation  
 3 (m, thick contours at 250 and 500 m) in northern Taiwan. The color scale is shown at the  
 4 bottom, and the contour at  $0.5 \text{ m s}^{-1}$  is not drawn. Old cells (A1, B1, and C1) and nearby new  
 5 cells (A2, B2) of interests are labeled. Green dashed lines AB and CD depict the vertical  
 6 cross-sections used in Fig. 11, and the short segments depict those used in Figs. 14-18 (blue  
 7 (brown) ones through B1 (C1)).



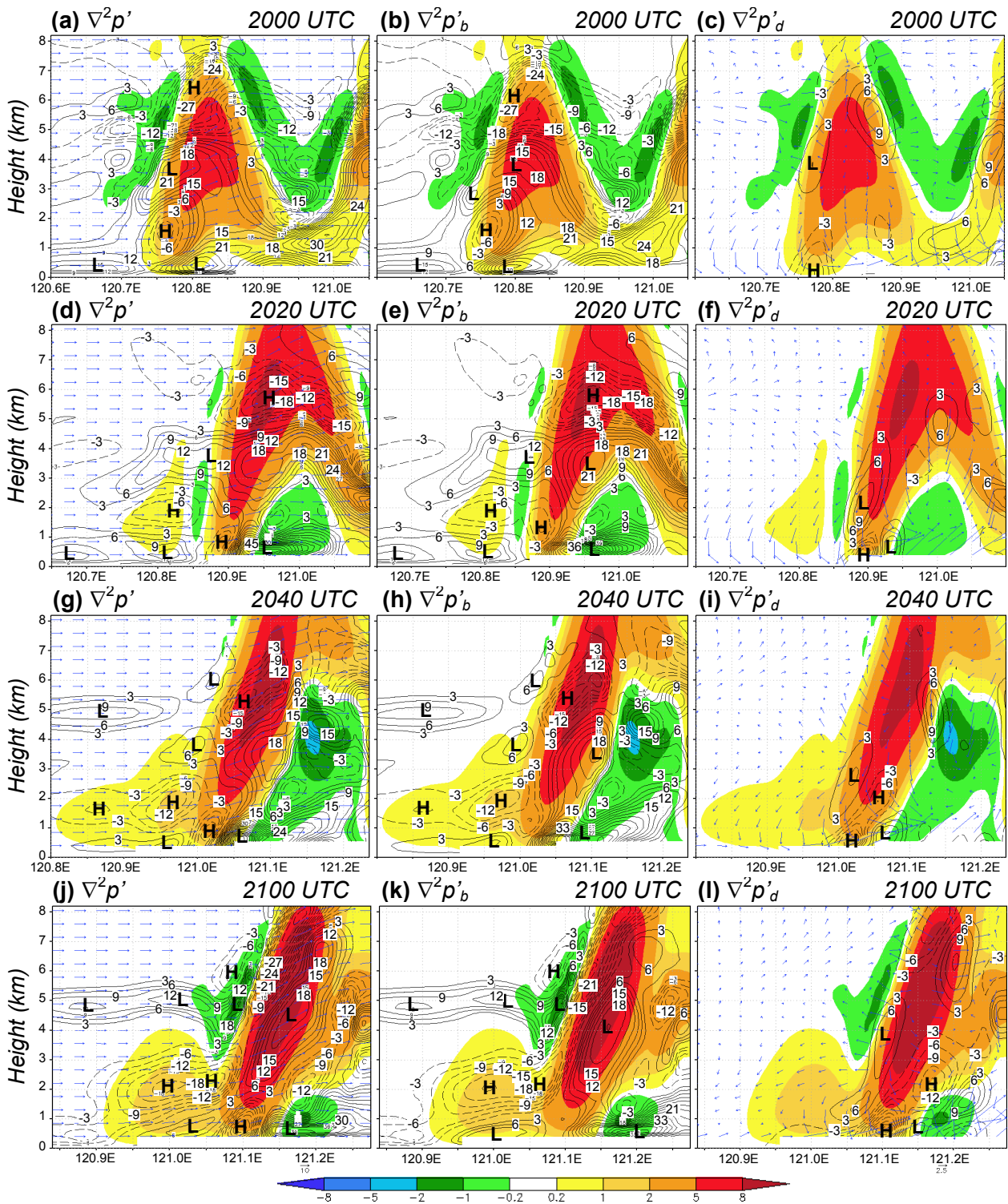
1 Figure 11. (a) E-W vertical cross-section of model-simulated convergence/divergence ( $10^{-4}$   
 2  $s^{-1}$ , color, positive for convergence) and  $\theta_e$  (K, contour, every 1 K) along  $25^\circ N$  (line AB in Fig.  
 3 10), averaged over 21:25-21:35 UTC 11 Jun 2012. The triangle marks the mean location of  
 4 the updraft of B1. (b, c) As in panel (a), except showing (b) convergence/divergence (color)  
 5 and wind vectors ( $m s^{-1}$ ) and speed (isotach every  $1 m s^{-1}$ ) and (c)  $w$  ( $m s^{-1}$ , color) and  
 6 vertical wind shear vector ( $10^{-3} s^{-1}$ , in cardinal direction, reference vectors both plotted)  
 7 along the WSW-ENE section (line CD in Fig. 10) at 21:00 UTC 11 Jun 2012. Thick  
 8 arrow-lines in (b, c) depict the axis of the LLJ.



1 Figure 12. CReSS simulation of convergence/divergence ( $10^{-4} \text{ s}^{-1}$ , shading, scale to the right,  
 2 positive for convergence), 10-m wind perturbation ( $\text{m s}^{-1}$ , green vectors, reference length at  
 3 bottom), and potential temperature perturbation ( $\theta'$ , K, contours every 0.1 K, dashed for  
 4 negative values) at the surface every 20 min from (a) 20:00 UTC to (f) 21:00 UTC 11 Jun  
 5 2012. Cells B1 (black) and B2 (blue), axis of convergence (thick dotted line) produced by  
 6 downdraft outflow of B1, and locations of vertical cross sections as in Fig. 10 (straight dashed  
 7 lines) are marked.

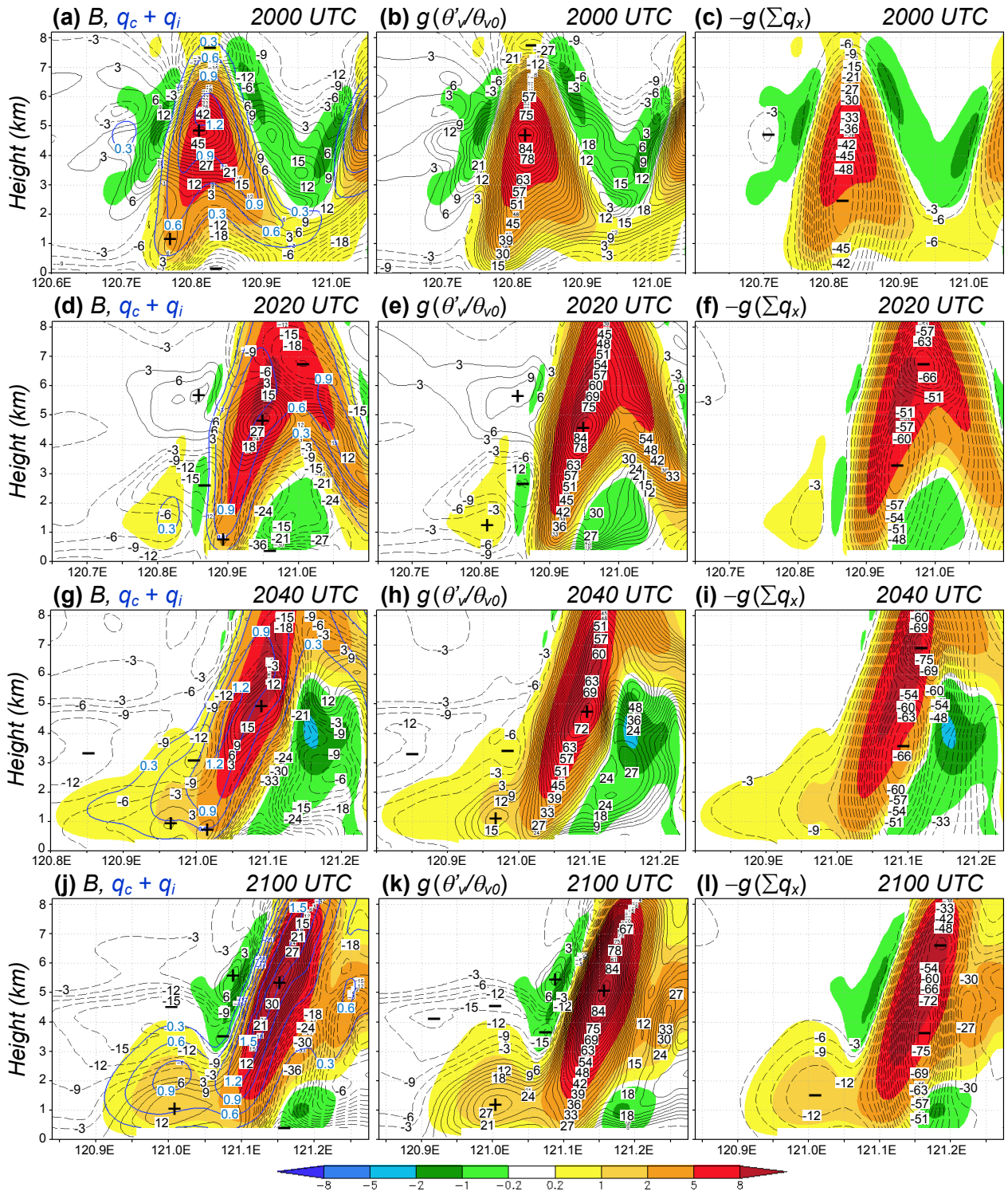


1 Figure 13. Model-simulated  $w$  ( $\text{m s}^{-1}$ , color, scale at bottom) and laplacian of perturbation  
 2 pressure ( $10^{-6} \text{ Pa m}^{-2}$ , contour, every  $3 \times 10^{-6} \text{ Pa m}^{-2}$ , dashed for negative values) of cells B1  
 3 and B2 at (left) 806 m and (right) 2929 m at 21:00 UTC 11 Jun 2012. (a, d)  $\nabla^2 p'$  obtained  
 4 from separation method, and (b, e)  $\nabla^2 p' = \nabla^2 p'_b + \nabla^2 p'_d$  and (c, f)  $\nabla^2 p'_b$  computed from Eqs.  
 5 (3) and (4). Cells B1 and B2 and updraft and downdraft centers are labeled in panels (a) and  
 6 (d).

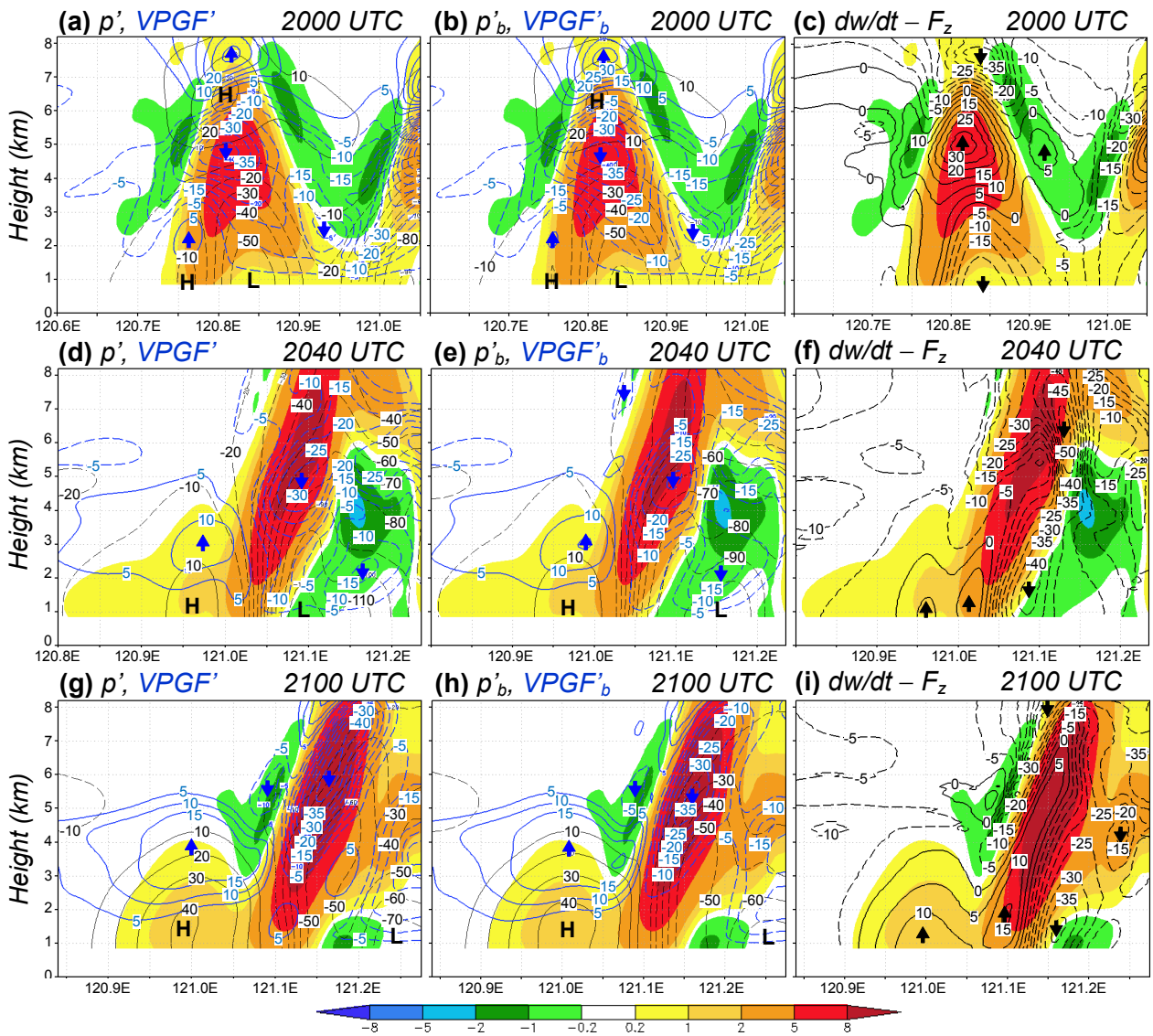


1 Figure 14. Vertical cross-sections of model-simulated  $w$  ( $\text{m s}^{-1}$ , color) and (a)  $\nabla^2 p'$  ( $10^{-6} \text{ Pa}$   
2  $\text{m}^{-2}$ ) and wind vectors ( $\text{m s}^{-1}$ , reference vector at bottom) on section plain, (b)  $\nabla^2 p'_b$   
3 (computed from Eq. 3), and (c)  $\nabla^2 p'_d$  (computed from Eq. 4) and vertical wind shear vector  
4 ( $10^{-3} \text{ s}^{-1}$ , in cardinal direction, reference vector at bottom) along the E-W segment through B1  
5 and B2 at 2000 UTC 11 Jun 2012 (cf. Fig. 10). All contour intervals are  $3 \times 10^{-6} \text{ Pa m}^{-2}$  (zero

- 1 line omitted, dashed for negative values), and letters H (L) denote corresponding high (low)
- 2 pressure perturbations. (d-f), (g-i), and (j-l) As in (a-c), except at 20:20, 20:40, 21:00 UTC
- 3 (WNW-ESE segments for 20:40 and 21:00 UTC, cf. Fig. 10), respectively.

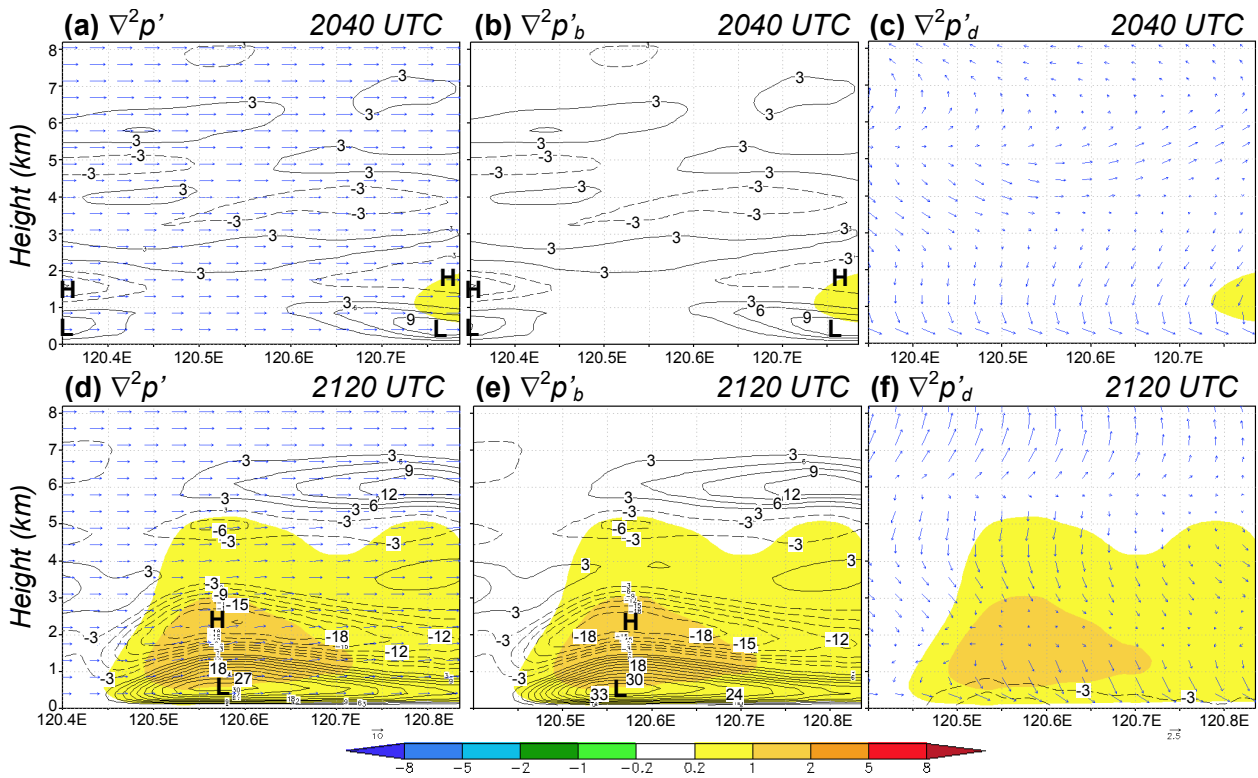


1 Figure 15. (a-c) As in Fig. 14a-c, but showing  $w$  and (a) buoyancy  $B$  ( $10^{-3} \text{ m s}^{-2}$ , black  
 2 contour) and mixing ratio of cloud particles ( $\text{g kg}^{-1}$ , blue contour, every  $3 \text{ g kg}^{-1}$ ), (b)  
 3  $g(\theta'_v/\theta_{v0})(10^{-3} \text{ m s}^{-2})$ , and (c)  $-g\Sigma q_x$  ( $10^{-3} \text{ m s}^{-2}$ ). All black contour intervals are  $3 \times 10^{-6} \text{ Pa}$   
 4  $\text{m}^{-2}$  (dashed for negative values, zero line omitted), and + (-) signs denote upward  
 5 (downward) maxima. (d-f), (g-i), and (j-l) As in (a-c), except at 20:20, 20:40, and 21:00 UTC,  
 6 respectively.

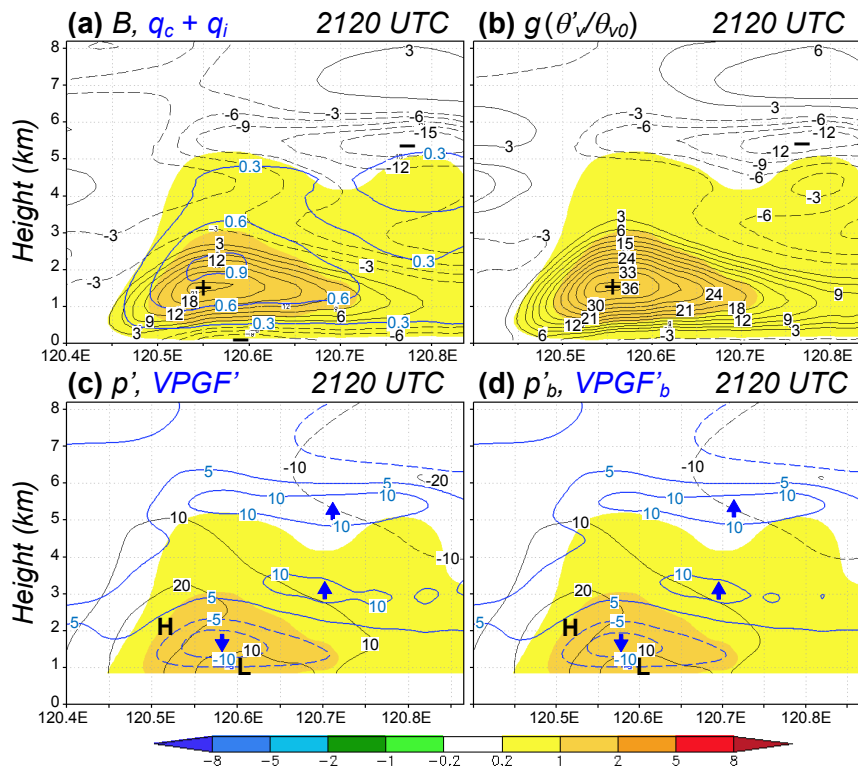


1 Figure 16. As in Fig. 14, but showing  $w$  and (a, d, g)  $p' = p'_b + p'_d$  (Pa, black contour, every  
 2 10 Pa, dashed for negative values) obtained from the relaxation method and the corresponding  
 3 perturbation PGF in the vertical ( $-(\partial p'/\partial z)/\rho_0$ ,  $10^{-3} \text{ m s}^{-2}$ , blue contour), (b, e, h)  $p'_b$  (Pa) and  
 4 its vertical PGF ( $10^{-3} \text{ m s}^{-2}$ ), and (c, f, i)  $dw/dt$  from vertical perturbation PGF and  $B$  ( $10^{-3} \text{ m}$   
 5  $\text{s}^{-2}$ , black contour). For force (per unit mass) and acceleration, all contour intervals are  $5 \times$   
 6  $10^{-3} \text{ m s}^{-2}$  (dashed for negative values), and upward (downward) arrows denote maxima  
 7 (minima).





1 Figure 17. As in Fig. 14, but showing  $w$  ( $\text{m s}^{-1}$ , color) and (a)  $\nabla^2 p'$  ( $10^{-6} \text{ Pa m}^{-2}$ ) and wind  
 2 vectors ( $\text{m s}^{-1}$ ) on section plain, (b)  $\nabla^2 p'_b$ , and (c)  $\nabla^2 p'_d$  and vertical wind shear vector ( $10^{-3}$   
 3  $\text{s}^{-1}$ , in cardinal direction) along the WSW-ENE segment through C1 at 20:40 UTC 11 Jun  
 4 2012 (cf. Fig. 10). (d-f) As in (a-c), except at 21:20 UTC.



1 Figure 18. (a, b) As in Fig. 15a and b, but showing  $w$  (color) and (a)  $B$  (black contour) and  
 2 mixing ratio of cloud particles (blue contour) and (b)  $g(\theta'_v/\theta_{v0})$  along the WSW-ENE segment  
 3 through C1 at 21:20 UTC 11 Jun 2012. (c, d) As in Fig. 16a and b, but showing  $w$  and (c)  $p'$   
 4 (black contour) obtain from the relaxation method and  $-(\partial p'/\partial z)/\rho_0$  (blue contour) and (d)  $p'_b$   
 5 and its vertical PGF along the segment as in panels (a, b) at 21:20 UTC.